

Montana Tech Library

Digital Commons @ Montana Tech

Graduate Theses & Non-Theses

Student Scholarship

Summer 2020

MONITORING THE 2018 ERUPTION OF KĪLAUEA VOLCANO USING VARIOUS REMOTE SENSING TECHNIQUES

Ninad Bhagwat

Follow this and additional works at: https://digitalcommons.mtech.edu/grad_rsched



Part of the [Geophysics and Seismology Commons](#)

MONITORING THE 2018 ERUPTION OF KĪLAUEA VOLCANO USING
VARIOUS REMOTE SENSING TECHNIQUES

By

Ninad Bhagwat

A thesis submitted in partial fulfillment of the
requirements for the degree of

Master of Science in Geoscience:
Geophysical Engineering

Montana Technological University

2020



Abstract

Monitoring the regions that are prone to natural hazards is essential in disaster management to provide early warnings. Airborne and space-borne remote sensing techniques are cost-effective in accomplishing this task. Interferometric Synthetic Aperture Radar (InSAR) is an advanced remote sensing technique used to detect and measure the changes in the Earth's topography over time. Spaceborne InSAR is a precise (~mm accuracy) way to measure the land surface altitudinal changes. Persistent Scatterer Interferometry (PSI) is a powerful method of differential SAR interferometry that processes the InSAR data by automatically selecting the persistent scatterers in the region. In this thesis, I developed a new algorithm to estimate the areal coverage and volume of newly erupted lava by integrating the space-borne InSAR, thermal infrared, Light Detection and Ranging (LiDAR), and Normalized Difference Vegetation Index (NDVI) techniques. I applied this algorithm to the eruption of the East Rift Zone (ERZ) of the Kīlauea volcano that took place between May and August 2018 as a case study, and estimated the areal coverage and volume of lava erupted. I compared the results of InSAR to those derived from airborne LiDAR. I found that although air-borne LiDAR provides data with higher resolution and accuracy, InSAR is almost as good as LiDAR in monitoring deformed areas and has larger spatial and temporal coverage. I also performed the PSI analysis using the Stanford Method for Persistent Scatterers (StaMPS) algorithm, and determined the Line-of-Sight (LOS) deformations prior, during, and after the 2018 eruption of the Kīlauea volcano. Results from the PSI processing show regional subsidence on the Big Island, indicating the deflation of the southern and western part of the Big Island during the eruption at the East Rift Zone.

Keywords: Kilauea, InSAR, Thermal, NDVI, PSI

Dedication

I would like to dedicate this thesis to my mother, who was always there for me when I was feeling down due to various reasons. I would also like to thank my father for providing financial support for some of my education.

Acknowledgements

As my work towards this thesis progressed, many people helped me. First of all, I would like to thank my advisor Dr. Xiaobing Zhou for mentoring me. I would also like to show my gratitude towards him for always encouraging me to try new things. I would also like to thank him for believing in me and taking me under his wings even when I was just recovering from a deadly illness and I did not have an extensive radar remote sensing background. Secondly, I would like to thank my committee members Dr. Mohammadhossein Sadeghiamirshahidi, Mr. Jeremy Crowley and Dr. Marvin Speece for their valuable comments and suggestions in making this project better. I would also like to thank the High-Performance Computer administrator Dr. Bowen Deng for his assistance in using the HPC and StaMPS software. I would like show my gratitude to the European Space Agency's STEP forum as well, for helping me learning the ESA SNAP and StaMPS software. Lastly, I would like to thank my fellow students Hubbel Rowe and Guohui Yao for their assistance with many features in MATLAB and ArcGIS.

Table of Contents

ABSTRACT	II
DEDICATION	III
ACKNOWLEDGEMENTS	IV
LIST OF TABLES	VII
LIST OF FIGURES	VIII
LIST OF EQUATIONS	XI
1. INTRODUCTION	1
2. GEOLOGIC BACKGROUND	6
3. DATA SOURCES AND METHODOLOGY	12
3.1. <i>Sentinel-1A InSAR</i>	12
3.1.1. Estimating the Volume of lava.....	13
3.1.2. PSI Analysis.....	15
3.2. <i>Landsat 7 & 8 Thermal Infrared and NDVI</i>	19
3.3. <i>Airborne LiDAR</i>	24
3.4. <i>Other Accessory Data</i>	26
4. ALGORITHM FOR ESTIMATING THE AREA AND VOLUME OF LAVA	28
5. RESULTS.....	36
5.1. <i>Estimated Area and Volume of Erupted Lava</i>	36
5.2. <i>Comparison between Vertical Displacements Derived from InSAR and LiDAR Analysis</i> ..	37
5.3. <i>PSI Analysis</i>	40
6. DISCUSSION	46
6.1. <i>Estimated Area and Volume of Erupted Lava</i>	46
6.2. <i>Comparison Between InSAR and LiDAR</i>	49
6.3. <i>LOS Displacement</i>	49

7. CONCLUSIONS..... 52

8. REFERENCES AND BIBLIOGRAPHY 54

List of Tables

Table I: Perpendicular and temporal baselines of all the Sentinel-1A SAR images used for this study. Baselines are referenced to the master image of April 20, 2018.....	15
--	----

List of Figures

- Figure 1: Map showing the Hawaiian archipelago and location of the Kīlauea crater, along with surrounding rift zones and Mauna Loa crater.7
- Figure 2: Flowchart for interferogram formation (Grassi and Mancini, 2019).14
- Figure 3: Flowchart for pre-processing of the interferometric stack (Grassi and Mancini, 2019)17
- Figure 4: Flowchart for StaMPS processing to generate the time-series (Hooper e al., 2012).19
- Figure 5: Landsat 8 thermal imagery of different dates. Bright white spots indicate presence of lava. (a) April 12, (b) May 14, (c) June 15, (d) July 1, (e) August 2.....21
- Figure 6: Landsat 7 thermal images with stripes of no data. (a) April 4, (b) May 22, (c) June 4, (d) July 9, (e) July 25, 2018.22
- Figure 7: Images shown in Figure 6 with strips of missing data recovered by the in-painting algorithm.23
- Figure 8: Combinations of temperature images generated by extracting the temperatures greater than or equal to 50°C from all the previous images. (a) Temperature image of May 14, (b) May 22, (c) June 07, (d) June 15, (e) July 01, (f), July 09, (g) July 25, (h) August 02, 2018.....23
- Figure 9: Map showing the difference in acquisition areas from both LiDAR surveys25
- Figure 10: Images showing location map of Puu’O’O crater and LiDAR data at the crater. Image resolution is set at 30m. LiDAR image courtesy: <https://opentopography.org/>26

- Figure 11: Map showing distribution of hot spots detected by VIIRS and Landsat 8 over the Kīlauea crater and East Rift Zone. The VIIRS data were acquired between May 13 and May 19, 2018, and the Landsat 8 image was acquired on May 14, 2018.27
- Figure 12: Flowchart of the procedure for estimating lava area and volume erupted.28
- Figure 13: Histogram for the temperature sensitivity analysis between temperatures 40°C and 95°C.29
- Figure 14: (a) Temperature (top panel) and NDVI (bottom panel) of the Kīlauea crater, (b) temperature (top panel) and NDVI (bottom panel) in the vegetated area in the Leilani Estates, (c) histogram of the clipped NDVI image.31
- Figure 15: (a) Temperature difference image shows that the Kīlauea crater and some other areas are masked and only lava has high temperature difference, (b) the histogram of the temperature difference image.32
- Figure 16: Sentinel-1A SAR images and Landsat 7 and 8 temperature and NDVI images used to estimate the volume of lava erupted. A double-arrow sign indicates a pair of images formed by a displacement image derived from SAR image and a thermal and NDVI images derived from Landsat 7 and 8 used together for lava volume estimation..34
- Figure 17: (a) Land area inundated by lava (in red) detected by my algorithm between May and August, 2018, (b) Vegetation destroyed in the eruption episode.....36
- Figure 18: Images showing the vertical difference derived from the LiDAR data between June and July 2018 (Left top), the vertical displacement image derived from InSAR between June 7 and July 13, 2018 (Right top), absolute difference image between InSAR and LiDAR data (Left bottom) and relative difference image between InSAR and LiDAR data

(Right bottom). The red circle in all images mark the area inside the Pu'u O O crater.
.....38

Figure 19: Histogram showing the relative difference between vertical displacement calculated by InSAR and LiDAR. Pixels with high percent difference are inside the Pu'u O O crater.
.....39

Figure 20: Graph showing the results of sensitivity analysis performed on the relative difference image between InSAR and LiDAR acquisitions. Yellow line represents the decline in the pixels with increasing relative difference, blue line represents the cumulative percentage of pixels with relative difference.40

Figure 21: Velocity map showing the area covered in my study.....41

Figure 22: Wrapped interferograms generated by StaMPS tool.42

Figure 23: Interferograms generated after phase unwrapping.42

Figure 24: Locations of the points selected for time series.43

Figure 25: Time series plots of the selected points.....44

Figure 26: Landsat 8 image of April 12, 2018 (Left) and Landsat image of April 12, 2018 superimposed by the shapefile created from the Landsat 8 image of September 19, 2018 (Right) showing the addition of new land due to cooling and solidifying of the erupted lava in the ocean. Shapefile was created visually.47

List of Equations

- (1) Absolute difference between InSAR and LiDAR derived vertical displacements..... 37
- (2) Relative difference between InSAR and LiDAR derived vertical displacements..... 37

1. Introduction

To mitigate severity of volcanic hazards, identification of volcanic activity is the primary goal of active volcano monitoring (Garthwaite et al., 2019). Monitoring volcanic activity can be carried out in many ways, such as studying earthquakes near the volcanoes, detecting various gases such as sulphur dioxide (SO₂) emissions, or detecting the bulging of ground using tilt meters, etc. Moreover, various remote sensing techniques enable researchers to observe and study the volcanoes remotely and quantitatively (De Novellis et al., 2017). The more frequently the monitoring data is collected, the higher the temporal resolution will be in monitoring the dynamical behaviors of volcanos.

Advanced remote sensing techniques can effectively acquire information about changes in elevation and shape of topographic features such as volcanic cone, crater dimensions, etc., and observe various natural phenomena, and examine the physical properties of the Earth surface (Grzesiak and Milczarek, 2018). Interferometric Synthetic Aperture Radar (InSAR) is an advanced remote sensing technique for monitoring the Earth's surface displacement over time, which is caused either by natural processes such as volcanic eruption, or by anthropogenic processes such as land surface subsidence due to groundwater overdraw or mining activities (Zhou et al., 2009; Lu et al., 2010; Jo et al., 2015b; Pepe and Calo, 2017; Lu et al., 2017; Grzesiak and Milczarek, 2018). Since SAR sensor actively emits radar waves and measures the reflected waves at the antenna, SAR is considered as an active sensor, as opposed to the thermal and optical sensors, which are considered as passive sensors. As an active sensor operating in the microwave region of the electromagnetic spectrum, Synthetic Aperture Radar (SAR) does not need any external energy source (solar radiation, for instance) and has a full day-and-night working capability (Pepe and Calo, 2017). SAR can work even under most precluding visual

conditions, such as presence of fog, clouds of thunderstorms, etc., since radar waves can penetrate through the clouds (Rowland et al., 1999). In addition, SAR images can detect both horizontal and vertical ground movements (Zhou et al., 2009; Lu et al., 2010). Interferometry is the process of forming an interferogram from two phase images. Interferograms, also referred to as SAR interferometric fringes, are formed by pairs of interferometric SAR phase images and contain information on changes in the slant range between the radar sensor and the ground. Radar illuminates a swath of the Earth's surface and records the backscattered power of the reflected radar waves. Deformation is measured by observing the phase difference between two phase images (Parks et al., 2011).

Differential Synthetic Aperture Radar Interferometry (DInSAR) is a set of InSAR processing techniques to obtain the deformation and the ground motion (Crosetto et al., 2015). DInSAR includes various InSAR processing methods, such as Small Baseline Subset (SBAS) (Baker and Amelung, 2012; Chen et al., 2014; Babu and Kumar, 2019), Persistent Scatterer (PS) (Hooper et al., 2007; Tofani et al., 2013; Bekési et al., 2019), Distributed Scatterer (DS) (Zhang et al., 2015; Lu et al., 2019) etc. Deformation is measured from the phase difference between at least two co-registered interferometric SAR images. Calculation of the phase difference is essential for the generation of the Digital Elevation Model (DEM). Removing noise from the calculated phase difference and obtaining only the phase change due to the ground displacement is a primary goal of the DInSAR processing techniques. Noise includes the phase change caused by the difference in perpendicular and temporal baselines between two acquisitions, due to atmospheric artifacts, due to surface properties such as moisture, and due to other reasons. After calculating the phase difference due to the ground motion, phase is converted into the displacement and further analysis is done.

Persistent Scatterer Interferometry (PSI) is a DInSAR technique to detect the ground deformation of the Earth's surface over time. PSI is a method that makes use of reflecting targets on the ground, that maintain a constant position over time. These targets produce high coherence upon coregistering two SAR images. PSI uses the multi-temporal acquisitions of the SAR data over the same area (Crosetto et al., 2015).

Estimating the area and volume of erupted lava is a critical component of monitoring volcanoes. Estimation of area and volume can help researchers understand and model the future lava flow directions and issue warnings. The volume of lava can be estimated by determining the InSAR or stereoscope derived Digital Elevation Model (DEM) difference. This technique was used on various occasions to estimate the volume of lava during the eruption at the Okmok volcano in 1997 using the European Remote Sensing (ERS) satellite and airborne Topographic Synthetic Aperture Radar (TOPSAR) imagery (Lu et al., 2003); at the Nyamulagira volcano in 2011-12 using the TanDEM-X InSAR derived DEMs (Albino et al., 2015); at the Pico do Fogo volcano in 2014-15 using the Pleiades-1 stereoscopic imagery and TanDEM-X InSAR imagery (Bagnardi et al., 2016); and, at the Kilauea volcano in 2018 using a single pass Ka band airborne InSAR imagery (Lundgren et al., 2019). The volume of lava from historic eruptions can also be estimated using this method. Lewis-Kenedi et al., (2005) estimated the total volume of lava flows at the Tequila volcanic field that occurred over a period of 1 million years using aerial photographs and DEMs. Field-based monitoring techniques can also yield estimates of volume. Stevens et al., (1996) estimated the lava volume at Mount Etna using the Electronic Distance Measurement (EDM) technique. A combination of in-situ, airborne and spaceborne sensing equipment can also help estimate the volume of lava. The volume of caldera collapse and the volume of erupted lava was estimated during the eruption of Kilauea volcano in 2018 using

ground-based GPS stations, tiltmeters, spaceborne InSAR (ALOS) and airborne LiDAR (Neal et al., 2019).

However, using the DEM difference to estimate the topographic changes, such as demonstrated by (Lu et al., 2003; Albino et al., 2015; Bagnardi et al., 2016; Lundgren et al., 2019) considers neither the deformation due to wildfires that are caused by lava flowing through forests, nor the deformation that might take place due to the presence of geothermal sources, earthquakes, or subsidence due to mining, oil and ground water overdraw, etc. Therefore, the estimate of change derived solely using the DEM difference might overestimate the volume. In addition, Hawaiian volcanoes are some of the best monitored volcanoes around the world, being in close proximity to the residents. The United States Geological Survey (USGS) and Hawaiian Volcano Observatory (HVO) have installed a wide network of GPS stations, tilt-meters, and seismometers on and near the Kīlauea volcano. HVO is continuously monitoring the activity at the Kīlauea crater and surrounding areas. However, some volcanoes in the world do not have monitoring stations installed yet, either because they are located at extremely remote areas, or because installing and maintaining monitoring stations at those volcanoes is not logistically feasible. Therefore, as of now, monitoring the eruptions at these other volcanoes might not be possible in the manner Kīlauea is being monitored. Using chartered flights to fly over volcanoes and conduct LiDAR surveys (USGS (2018a; 2018b)) or InSAR acquisitions (Lundgren et al., 2019) to monitor the eruptive episode might not be possible or affordable every time either.

Therefore, my objective was to develop a general method to estimate the areal coverage and volume of lava erupted solely using freely available and open source data from space-borne instruments. The method was focused on estimating the volume by removing the other sources of deformation, such as earthquakes, groundwater overdraw, wildfires, or geothermal areas. I

applied this method to the 2018 eruption of the Kīlauea volcano as a case study. I compared results from the InSAR processing to those derived from airborne LiDAR to check the accuracy of InSAR processing. My other objective was to analyze the pre-, co- and post-eruption deformations of the eruption of Kīlauea volcano in 2018 using Persistent Scatterer Interferometry and derive the time series at several key locations, and thereby determine the regional correlation in deformation relative to the eruption.

2. Geologic Background

The islands of Hawaii in the Northern Pacific Ocean are home to many volcanoes, including Kīlauea, Mauna Loa, Mauna Kea, etc. Hawaiian volcanoes are considered as some of the most active ones around the world. The islands were formed due to ‘hot spot’ volcanism (Morgan, 1971). With highly basaltic composition, lava erupted by the Hawaiian volcanoes tends to be highly mobile and has been observed to be travelling great distances, before finally flowing into the Pacific Ocean (Shaw et al., 1968). Kīlauea volcano is situated at the southern part of the Big Island. It is a shield volcano that has a shallow magma plumbing system (Neal et al., 2019). Kīlauea is currently the youngest and most active volcano in the chain of the Hawaiian volcanoes. Kīlauea is also one of the most active volcanoes around the world, providing a natural laboratory for studying the volcanic process and volcanism (Baker and Amelung, 2012). The influence area of the Kīlauea volcano consists of a summit caldera (which homes the Halema‘uma‘u crater) and two rift zones viz. the South Western Rift Zone (SWRZ) and the East Rift Zone (ERZ) (Zhai and Shirzaei, 2016). The Kīlauea volcano has been active since 1983, with major lava effusions taking place from the Puu‘O‘O crater on the East Rift Zone (ERZ), situated at approximately 18 km at east of the Kīlauea’s summit caldera (Heliker et al., 2003).

Beginning March 2018, high seismic activity and ground bulging started to take place on the ERZ (Neal et al., 2019). Following the collapse of the Puu‘O‘O crater on April 30, lava effusion started on May 3 at Leilani Estates at the Northeast side of the Puu‘O‘O crater. The eruption, combined with a 6.9 magnitude earthquake occurred on May 4, 2018, opened many new fissures along the East Rift Zone (ERZ) of the volcano, threatening the residents of the area. Early hazard warnings were issued by the Hawaiian Volcano Observatory (HVO) based on the tiltmeter readings. After the first eruptive activity ended, fissure activity started again on May 12,

2018. In late May, the Halema‘uma‘u crater at the summit caldera also collapsed, possibly due to the withdrawal of magma from the crater to supply the vigorous lava effusion of the eastern side of the crater (Babu and Kumar, 2019). The eruption activity continued for three months until August 4, 2018, when it stopped abruptly (Babu and Kumar, 2019; Neal et al., 2019).

Based on the Light Detection and Ranging (LiDAR) derived vertical differencing data, the volume collapse of the summit caldera was estimated to be between 0.825 km^3 to possibly more than 1 km^3 (Neal et al., 2019). The volume of the subaerial lava effusion was estimated to be 0.593 km^3 , based on the acquisitions from the Ka band airborne InSAR (Lundgren et al., 2019). About 3.78 km^2 of new land was added to the eastern side of the Big Island (Babu and Kumar, 2019) due to flow and accumulation of the erupted lava in the Pacific Ocean. A location map of the Kīlauea volcano can be seen in Figure 1.



Figure 1: Map showing the Hawaiian archipelago and location of the Kīlauea crater, along with surrounding rift zones and Mauna Loa crater.

The eruption of Kīlauea volcano in 2018 was monitored using various remote sensing techniques. Babu and Kumar (2019) performed a Small Baseline Subset (SBAS) analysis and an

InSAR coherence analysis of the 2018 Lower East Rift Zone (LERZ) eruption using the Sentinel-1A data. Lundgren et al. (2019) determined the topographic changes due to the 2018 eruption of the Kīlauea volcano using a single-pass airborne InSAR instrument. Neal et al. (2019) monitored the LERZ eruption of 2018 using Global Positioning System (GPS), InSAR, and LiDAR datasets.

Many other studies have also been carried out on the Kīlauea volcano and the Lower East Rift Zone using various geodetic and remote sensing methods. Rowland et al. (1999) analyzed topographic data from a C-band interferometric airborne radar, collected in September 1993 and determined the accuracy of the Terrain Observation with Progressive Scan SAR (TOPSAR) data by comparing it with field observations and previous Digital Elevation Models (DEMs). Flynn et al. (2001) demonstrated the use of Landsat thermal imagery to measure the effusion rates over Kīlauea and some other volcanoes. Mougini-Mark and Garbeil (2005) compared the PacRim-2 airborne SAR and airborne LiDAR data to determine the difference in results between TOPSAR and LiDAR. Baker and Amelung (2012) utilized Radarsat-1 data to perform the SBAS time-series analysis on the Summit caldera of the Kīlauea volcano between 2000 and 2008. Richter et al. (2013) used TerraSAR-X interferometry and LIDAR to identify and analyze the small-scale deformation near the new vent that had formed due to a small explosive eruption at the summit of the Kīlauea volcano. Shirzaei et al. (2013a) derived the aseismic slip across the Hilina Fault System, which is located at the southern flank of the Kīlauea volcano, using InSAR and wavelet analysis of InSAR and GPS. Chen et al. (2014) used TerraSAR-X data to study the slow slip event of the Kīlauea volcano in 2010 using the SBAS technique. Poland (2014) used TanDEM-X to derive the DEMs for determining the discharge rates of subaerial lava flow at the Kīlauea volcano between September 2011 and March 2013. Jo et al. (2015a) used COSMO-SkyMed X

band sensor and integrated stacking and multiple aperture interferometry techniques to detect the location of the new intrusion of magma beneath the Summit Caldera of the Kīlauea volcano in 2015. Jo et al. (2015b) applied the Cosmo-SkyMed X band interferometric data to analyze the surface deformation during the Kamoamoā fissure eruption of the Kīlauea volcano in March 2011. Zhai and Shirzaei (2016) developed a spatio-temporal model of the Kīlauea's summit magmatic system using ENVISAT satellites and performing wavelet based InSAR and time series inversion. Jo et al. (2017) used the TerraSAR-X data and Multiple Aperture Interferometry (MAI) technique to determine the three-dimensional volcanic deformation at the Kīlauea volcano. Thompson and Ramsey (2020) compared the remotely sensed thermal data between 2017 and 2018 and performed an uncertainty analysis of the temperature of the lava.

Apart from the Kīlauea volcano, InSAR and other satellite imaging techniques have been previously used to monitor and analyze the dynamics of volcanism at various locations. Lu et al. (1997) determined the deformation of the New Trident volcano from an InSAR analysis using the ERS-1 data. Sigmundsson et al. (1999) deduced the mechanism of eruption of the Piton de la Fournaise volcano in March 1998 using the RADARSAT-1 data. Lu et al. (2000) used satellite radar interferometry to model the aseismic inflation at the Westdahl volcano in Alaska. Lu et al. (2004) estimated the average thickness of the 1991-1992 lava flow and prepared flow maps at the Westdahl volcano in Alaska using the Shuttle Radar Topography Mission (SRTM) DEM data and optical imagery. Poland and Lu (2008) utilized SAR data from many instruments to determine the displacements at Mount St. Helens during pre- and co-eruptive periods. Brunori et al. (2012) investigated the deformation at the Cerro Blanco / Robledo Caldera over the time span of 20 years. Wessels et al. (2012) monitored the Redoubt volcano during its unrest and eruption period of 2008-2009 using various satellite and airborne thermal infrared instruments. Ji et al.

(2013a) modelled the pre-eruption dyke intrusion at the Kizimen volcano in Russia using data from ENVISAT and ALOS PALSAR. Ji et al. (2013a) performed the SBAS analysis at the Agung volcano in Indonesia between 2007 and 2009 using the ALOS PALSAR data. Pritchard et al. (2014) monitored the non-eruptive background seismicity at different volcanoes of potential activity in Chile and Bolivia using ENVISAT InSAR and Advanced Space-borne Thermal Emission and Reflection Radiometer (ASTER) thermal data. Chen et al. (2017) combined the InSAR and Global Navigation Satellite System (GNSS) network to estimate the displacements at the Piton de la Fournaise volcano between 2009 and 2014. Coppola et al. (2017) determined the effusion rates of obsidian lava flows using the Moderate Resolution Imaging Spectroradiometer (MODIS) thermal data. De Novellis et al. (2017) used the DInSAR deformation maps derived from the Sentinel-1A SAR data and pre-eruptive time-series from the ENVISAT SAR data to model the source for the Wolf volcano eruption in 2015. Wnuk and Wauthier (2017) applied InSAR inversion to model the depth of magma sources that led to the 2014 Pacaya volcano eruption. Grzesiak and Milczarek (2018) used the SBAS-InSAR technique to determine the line-of-sight displacements at the Mauna Loa volcano between 2015 and 2017. Gonzalez et al. (2018) used Sentinel-1A InSAR imagery to model the eruption at the Pico de Fogo volcano in 2014. Kereszturi et al. (2018) combined airborne hyperspectral and LIDAR imagery to map the Tongariro Volcanic Complex after the eruptions of Te Maari in 2012. Kobayashi (2018) modelled the possible source of future phreatic eruption at the Midagahara volcano in Japan using the Advanced Land Observation Satellite (ALOS) imagery. Wang et al. (2018) utilized ENVISAT and TerraSAR-X data to estimate the surface deformation of the Akutan volcano between 2003 and 2016. Garthwaite et al. (2019) demonstrated a cost-effective method of combining InSAR and GNSS data to monitor volcanoes such as Rabaul Caldera in Papua New

Guinea. Plank et al. (2019) determined the topographic changes of a lava dome during the eruption of the Kadovar volcano in 2018-2019 using various satellite imagery.

Persistent Scatterer Interferometry has been widely used in various applications, from measuring ground subsidence due to human activities (Bekési et al., 2019) to determining hydraulic head changes and aquifer properties (Boni et al., 2016), to monitoring landslides (Tofani et al., 2013) to assessing volcanic deformation (Hooper et al., 2007; Ji et al., 2013b). Hooper et al., (2007) used the European Remote Sensing (ERS-1 and ERS-2) data and Stanford Method of Persistent Scatterers (StaMPS) method to detect two distinct sources of deformation at the Volcan Alcedo volcano in the Galapagos Archipelago; one caused by crystallizing of the magma chamber, and the other due to a landslide. Ji et al., (2013b) measured the deformation at Changbaishan Tianchi volcano between 2004 and 2010 using the ENVISAT Advanced Synthetic Aperture Radar (ASAR) images and PSI analysis. Tofani et al., (2013) used the PSI technique and in-situ geotechnical monitoring to characterize and monitor the landslide at Santo Stefano d'Aveto using the using the ERS-1, ERS-2 and ENVISAT satellites. Boni et al., (2016) used the PSI technique to derive the relation between ground motion and corresponding hydraulic changes in the London Basin using the data from ERS-1, ERS-2 and ENVISAT satellites. Bekési et al., (2019) implemented the ENVISAT satellite data and PSI method to monitor the subsidence due to fluid extraction at the geothermal field of Los Humeros during 2003 and 2007.

3. Data Sources and Methodology

3.1. Sentinel-1A InSAR

European Space Agency (ESA)'s Copernicus program consists of a family of missions designed to observe the Earth from various space-borne instruments (Balsamo et al., 2018). Under this program, ESA has launched constellations of Sentinel-1, Sentinel-2, Sentinel-3, and Sentinel-5P satellite with future plans to launch Sentinel-4, Sentinel-5 and Sentinel-6. Each satellite or satellite constellation has different features onboard and different applications. The constellation of Sentinel-1A and Sentinel-1B satellites provides SAR data of high resolution ($5\text{ m} \times 20\text{ m}$). The mission has an expected planned lifespan of 20 years with future plans of launching Sentinel-1C and Sentinel-1D, expanding the satellite constellation and reducing the time gap of data acquisition (Li et al., 2016). Sentinel-1 satellites orbit the Earth in a near-polar, sun synchronous orbit at approximately 700 km altitude with the revisit time of 12 days. SAR data available from Sentinel-1 is in the C-band of 5.56 cm wavelength. The images are downloadable from the ESA website (<https://perma.cc/E8QU-6828>). The data is updated frequently. Sentinel-1 satellites acquire data in four different modes: Strip-map mode (SM), Interferometric Wide mode (IW), Extra-Wide mode (EW), and Wave (WV). Data collected in each mode have unique properties and are used for different purposes. The satellites provide different types of images, including Single Look Complex (SLC), Ground Range Detected (GRD), and Ocean (OCN) images (Torres et al., 2012).

For this research project, I used the SLC images in the IW mode of the Sentinel-1A satellite, since SLC images retain both amplitude and phase information, as opposed to other types. Each SLC image is divided into three sub-swaths, since the satellite captures data in three sub-swaths using Terrain Observation with Progressive Scans SAR (TOPSAR) technique.

Orbiting around the Earth, satellite acquires one image in an ascending node, and acquires subsequent image in a descending node. Therefore, part of the area of interest lied either in the 1st or 3rd sub-swath of the image (2nd sub-swath was common). For this study I used the images from ascending node, in which the area of interest (AOI: Kīlauea crater, Mauna Loa crater, and ERZ) lied in the 2nd and 3rd sub-swaths. Procedures for the interferogram processing are explained below.

3.1.1. Estimating the Volume of lava

Along-track SAR interferometry is a remote sensing technique, where the observations of AOI are made from the same sensor position but at different times (Pepe and Calo, 2017). I used Along-track interferometry to manually generate 10 interferograms from 11 SAR images acquired between April, 2018 and August 18, 2018 that covered the 2018 Kīlauea volcano eruption period. All interferograms were referenced to the master image, acquired on April 20, 2018 before the eruption. Interferogram processing was implemented using the ESA SNAP software using an algorithm developed in (Braun and Veci, 2020). A flowchart of SAR data processing is shown in Figure 2.

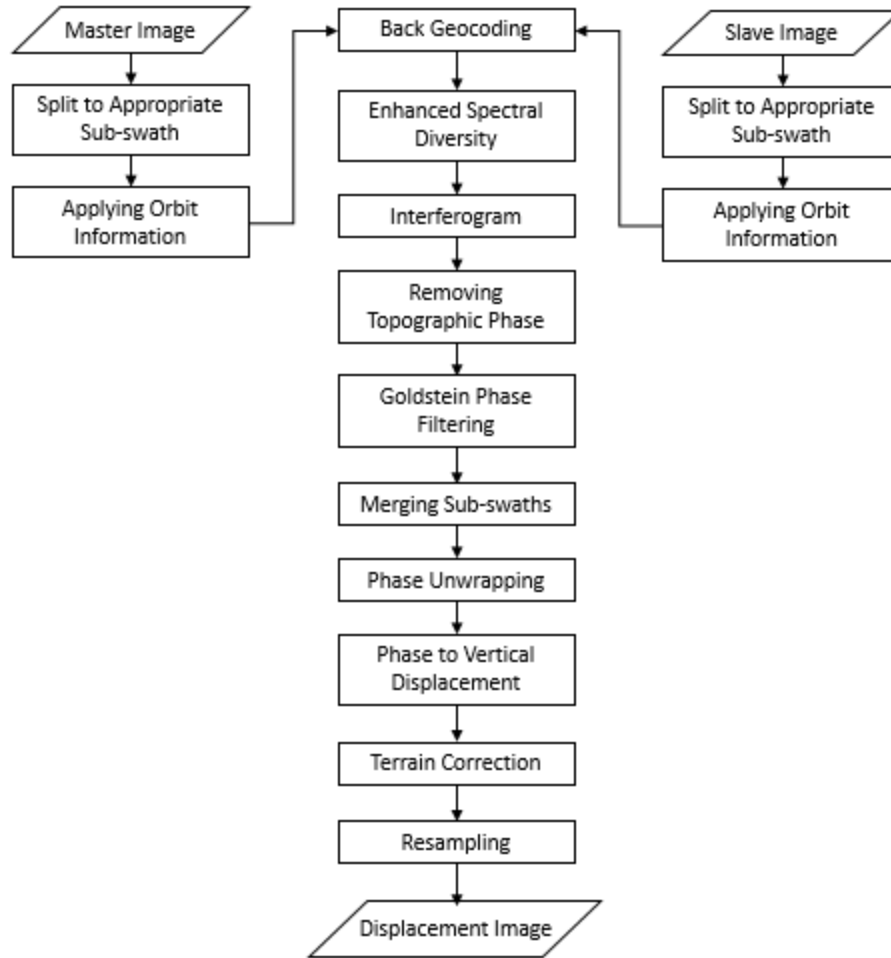


Figure 2: Flowchart for interferogram formation (Grassi and Mancini, 2019).

Aforesaid flowchart (Figure 2) is explained here briefly: First, I split each image into sub-swaths; then I applied the orbital information and coregistered the same sub-swaths of two images to form an interferometric pair from which, an interferogram was generated. While forming the interferogram, I removed the topographic phase using the DInSAR algorithm. After that, I filtered the interferogram using the Goldstein Phase Filter to reduce noise (Goldstein & Werner, 1998). Once the de-noised interferogram for one sub-swath was acquired, I repeated the same procedure for the second sub-swath. Then I merged the two sub-swaths to obtain one complete image of the area of interest. Phase unwrapping of the interferograms was performed

using Statistical Cost-Network Flow Algorithm for Phase Unwrapping (SNAPHU) (Chen and Zebker, 2002), in which, the Minimum Cost Flow (MCF) algorithm was used for phase unwrapping. The I converted the unwrapped interferograms into vertical displacement and then applied terrain correction. Since C band SAR images experience severe decorrelation issues in vegetated areas (Kervyn, 2001), phase unwrapping may have contained some errors. Therefore, many pixels in the displacement image had missing values, which the software termed NoData values. I interpolated the values of these pixels using the cubic convolution method.

3.1.2. PSI Analysis

I used a total of seventeen interferometric SAR images acquired by Sentinel-1A between March 03, 2018 and September 23, 2018 with the relative orbit number 124. Table I shows the perpendicular and temporal baselines of the Sentinel-1A SLC SAR images used in this study.

Table I: Perpendicular and temporal baselines of all the Sentinel-1A SAR images used for this study. Baselines are referenced to the master image of April 20, 2018.

Datasets	Polarization	Perpendicular Baseline [m]	Temporal Baseline [days]	Coherence
04/20/2018 - Master	VV	0.00	0.00	1.00
03/03/2018 - Slave	VV	-49.25	48.00	0.92
03/15/2018 - Slave	VV	-14.91	36.00	0.95
03/27/2018 - Slave	VV	-4.87	24.00	0.97
04/08/2018 - Slave	VV	-14.50	12.00	0.98
05/02/2018 - Slave	VV	16.75	-12.00	0.97
05/14/2018 - Slave	VV	-87.19	-24.00	0.91
05/26/2018 - Slave	VV	-93.86	-36.00	0.89
06/07/2018 - Slave	VV	-28.03	-48.00	0.93
06/15/2018 - Slave	VV	-16.92	-60.00	0.93
07/01/2018 - Slave	VV	19.01	-72.00	0.92
07/13/2018 - Slave	VV	19.68	-84.00	0.91
07/25/2018 - Slave	VV	-24.48	-96.00	0.89
08/06/2018 - Slave	VV	-45.33	-108.00	0.87
08/18/2018 - Slave	VV	-79.39	-120.00	0.83
09/11/2018 - Slave	VV	-13.46	-144.00	0.86
09/23/2018 - Slave	VV	-18.57	-156.00	0.84

Coherence between two interferometric SAR images in an interferometric stack decreases as the perpendicular baseline between them increases. Table I shows that the maximum perpendicular baseline was 93.86 m between the pair of April 20 and May 26, 2018. The lowest coherence of 0.83 is observed between the pair of April 20 and August 18, 2018. Still, coherence in all pairs was greater than 0.8. Therefore, all interferometric pairs resemble high coherence and hence, correlation between the master and slave images is very good (Lu et al., 2018).

I generated sixteen images of interferogram for PSI method. The PSI method requires all the interferograms be generated based on the single master image. I selected the master image that was acquired on April 20, 2018, since this image was the last image acquired by Sentinel-1A before the collapse of the Puu'O'O crater on April 30, 2018 (Neal et al., 2019). Pre-processing of the interferometric pairs was done in ESA SNAP software. I used an algorithm developed by (Grassi and Mancini, 2019) for pre-processing of interferograms. Workflow of pre-processing is very similar to that explained in section 3.1.1. I split each image into the sub-swaths. Then I generated the single master stacks from the split images for both sub-swaths. Then I generated the stacks of single master interferograms for both sub-swaths. I removed the phase due to existing topography during the formation of interferograms using the DInSAR algorithm. To reduce the noise from the interferograms, I applied a filtering algorithm developed by Goldstein and Werner, (1998). After forming the interferometric stacks for both sub-swaths with topographic phase removed and noise removed, I merged both stacks to create the stack for the whole AOI. To expedite the data processing, I cut the area of the merged stack to fit only the area of interest, thereby reduced the size of data. Once the required stack of interferograms was obtained, I converted it to StaMPS format using the snap2StaMPS algorithm developed by

Foumelis et al. (2018). A flowchart for pre-processing of interferogram for StaMPS processing is shown in Figure 3.

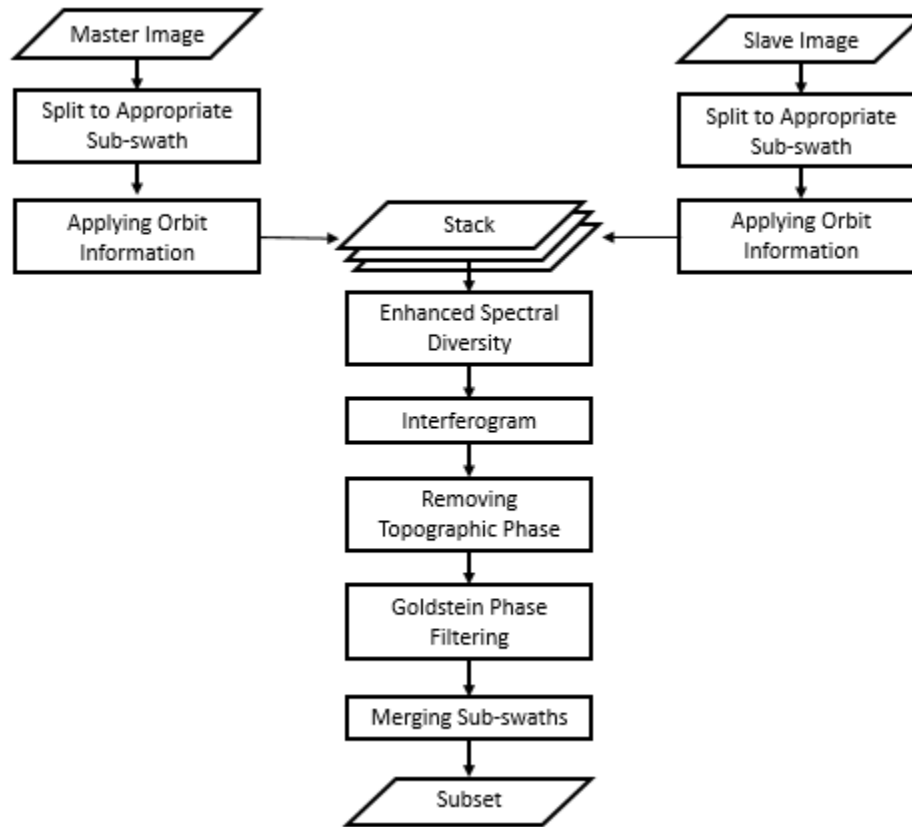


Figure 3: Flowchart for pre-processing of the interferometric stack (Grassi and Mancini, 2019)

I used the StaMPS algorithm developed by Hooper et al., (2012) to process the coregistered stack of the de-noised interferograms and get the displacement values. StaMPS uses the stack of the interferograms, converted by the snap2StaMPS algorithm (Foumelis et al., 2018). In the first step, StaMPS automatically converts the input data into the formats required for the PS processing. In addition to the filtering performed using the Goldstein Phase Filter (Goldstein and Werner, 1998) in the pre-processing step, StaMPS estimates and removes the phase noise in its second step. Once the noise from the interferograms is estimated, the persistent scatterers (PSs) are selected by StaMPS algorithm based on their noise characteristics, i.e. signal-to-noise

ratio. After appropriate PSs are selected, the pixels are filtered once again and the ones which are considered too noisy are excluded from further consideration. Once the PS pixels are selected, their wrapped phase is corrected for the spatially-uncorrelated look angle error (DEM error). Once the de-noised and filtered interferograms are obtained, phase unwrapping is carried out. After unwrapping, the spatially-correlated look angle error is again estimated and phase unwrapping can be redone with the newly estimated look angle error subtracted from the wrapped phase. Removing the look angle error and the orbital ramps can be carried out iteratively with increasing accuracy.

After the phase unwrapping, I filtered the phase due to atmospheric artifacts such as tropospheric delay, using the Toolbox for Reducing Atmospheric InSAR Noise (TRAIN) algorithm developed by Bakaert et al., (2015). TRAIN has been integrated with StaMPS so no format conversion was required. A Phase-based linear tropospheric correction was used to estimate and filter the phase due to atmospheric artifacts. Once the atmospheric phase correction was implemented, the StaMPS processing was complete and the interferometric stack was ready for analysis. A flowchart for the StaMPS algorithm is shown in Figure 4.

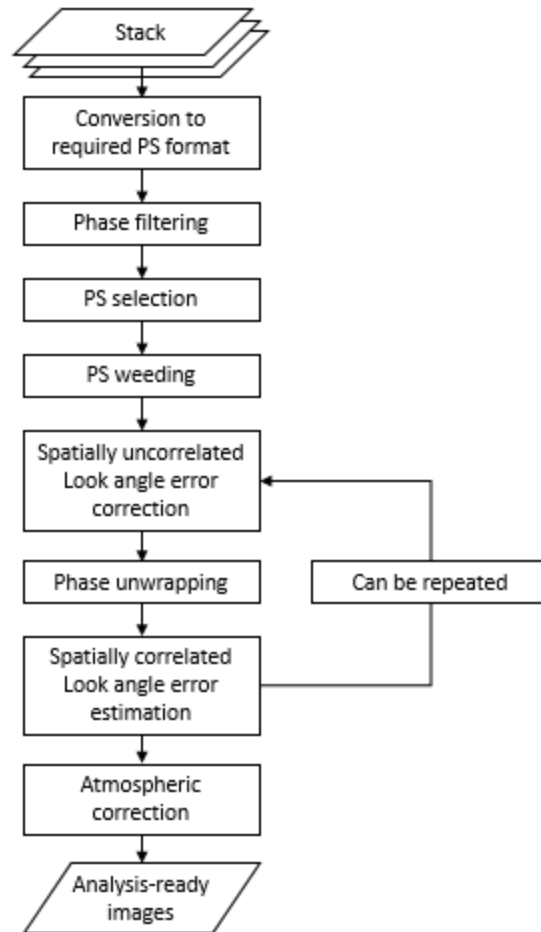


Figure 4: Flowchart for StaMPS processing to generate the time-series (Hooper et al., 2012).

3.2. Landsat 7 & 8 Thermal Infrared and NDVI

The Landsat program started in 1970s. The program currently has a global record of the Earth's surface for almost 50 years (Wulder et al., 2012). Currently, Landsat 7 and Landsat 8 are operational and provide a wide range of imagery for various applications. Landsat 7, carrying the Enhanced Thematic Mapper Plus (ETM+) sensor, was launched on April 15, 1999 and is expected to be operational until December 2020 after which, it will be decommissioned and replaced by Landsat 9. Landsat 8 carrying the Operational Land Imager (OLI) and the Thermal Infrared Sensor (TIRS) was launched on February 11, 2013 and is expected to operate for 10

years. Both Landsat 7 and Landsat 8 have a revisit time of 16 days with 8 days offset (Flood, 2014). Both satellites have similar spatial resolutions for the Visible Near Infrared (VNIR – 30 m), Short Wave Infrared (SWIR – 30 m) bands and panchromatic band (15 m). Spatial resolution of the thermal infrared bands for Landsat 7 (Band 6 – VCID 1 & 2) is 60 m, while that of the thermal bands of Landsat 8 (Bands 10 & 11 of TIRS) is 100 m. All images for distribution are resampled to 30 m spatial resolution.

For this study, I used a total of eleven Landsat 7 and Landsat 8 thermal images between April and August 2018, downloaded from the USGS's Earthexplorer data portal (<https://perma.cc/9U7V-YA7Y>). Temperature data from their respective thermal infrared bands were used for locating the active lava, since the lava has much higher temperature than the background. I selected a Landsat 7 image acquired on April 4, 2018 and a Landsat 8 image acquired on April 12, 2018 as references for temperature change analysis. I converted the original Digital Number (DN) values of the Landsat 7 band 6 VCID1 (thermal band) to the Top of the Atmosphere (TOA) brightness temperature (Landsat 7 Users Handbook). Similarly, the DN values of the band 10 of Landsat 8 were converted to TOA brightness temperature (Ihlen, 2019). I then converted the TOA brightness temperature into land surface temperature (LST) using the method developed by Avdan and Jovanovska (2016). Figure 5 shows the hotspots detected by Landsat 8 on April 12, May 14, June 15, July 1 and August 2, respectively.

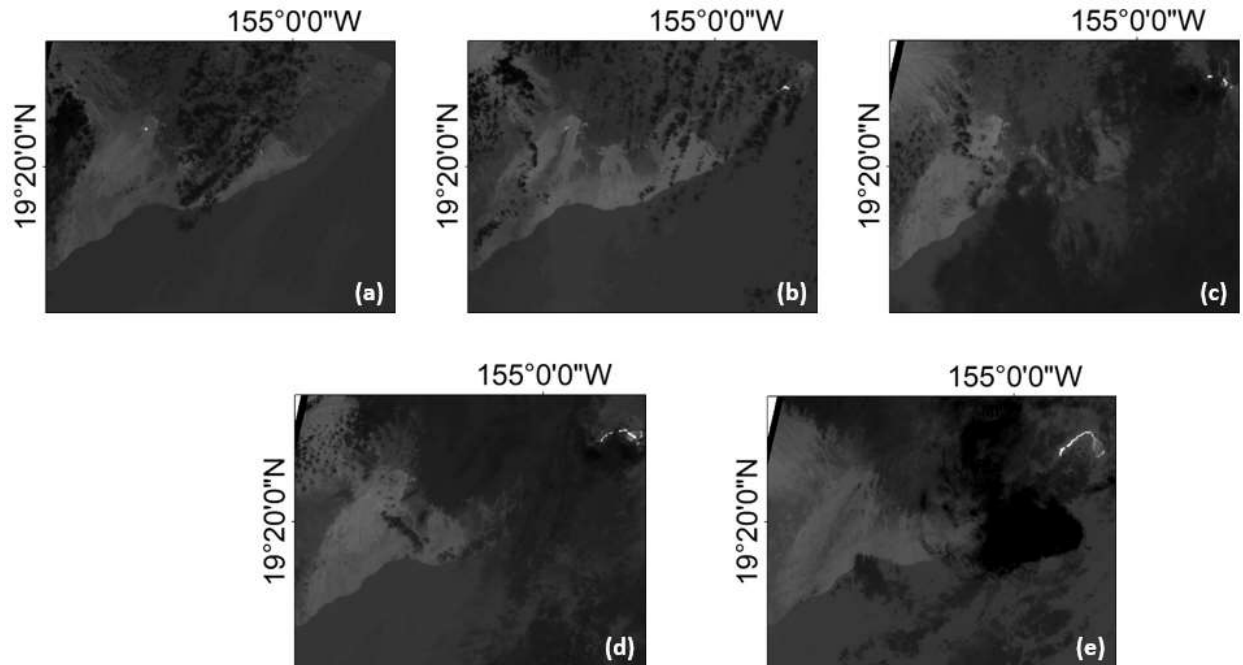


Figure 5: Landsat 8 thermal imagery of different dates. Bright white spots indicate presence of lava. (a) April 12, (b) May 14, (c) June 15, (d) July 1, (e) August 2.

I processed the bands 4 and 5 of Landsat 8 Optical Land Imager (OLI) and bands 3 and 4 of Landsat 7 Enhanced Thematic Mapper+ (ETM+) to produce the NDVI images. The NDVI images were used to determine if the area was vegetated or bare ground.

I used the thermal and NDVI images from both the Landsat 7 and Landsat 8 to reduce the time gap of acquisitions so that the temperature and vegetation changes with time can be more closely monitored. However, for Landsat 7 images, breakdown of the Scan Line Corrector (SLC) on May 31, 2003 has resulted in strips of missing data in images of all bands. Figure 6 shows the Landsat 7 thermal images of April 4, May 22, June 7, July 9, and July 25, 2018. Strips of missed data are clearly visible.

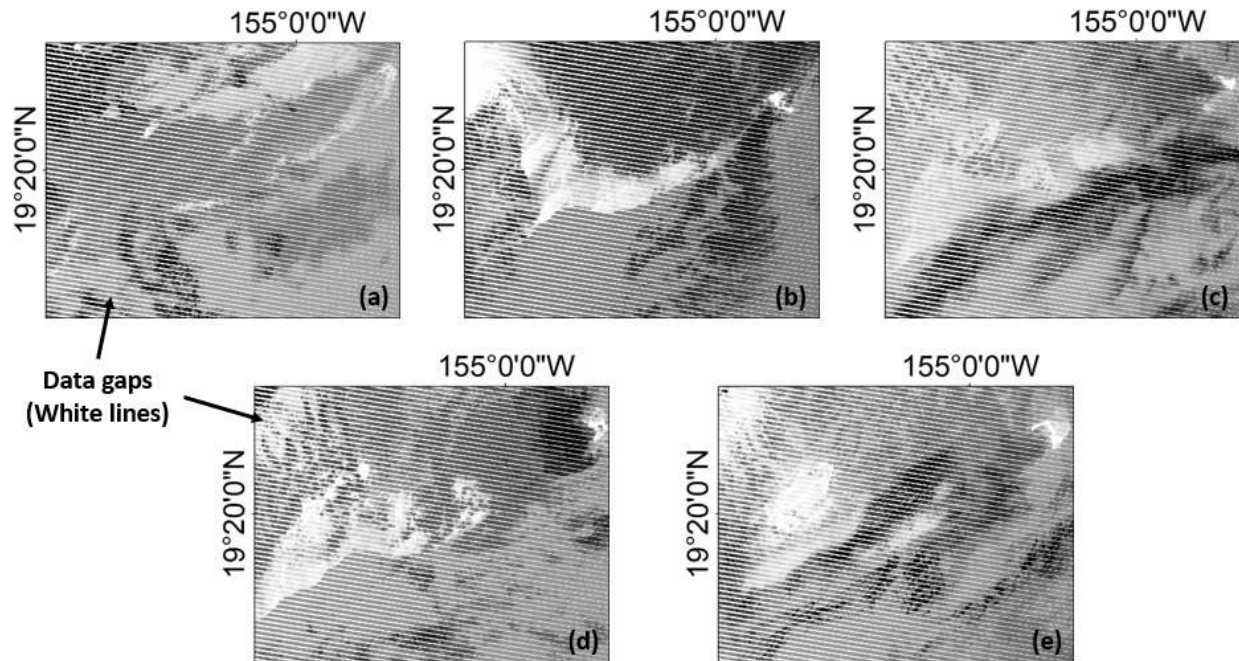


Figure 6: Landsat 7 thermal images with stripes of no data. (a) April 4, (b) May 22, (c) June 4, (d) July 9, (e) July 25, 2018.

Missing strips of Landsat 7 data were recovered on request by Dr. Jiaqing Miao using the In-painting algorithm developed by Miao et al., (2019). Figure 7 shows the corresponding Landsat 7 thermal images of Figure 6 with missing strips recovered using the inpainting algorithm. Missing data strips in the NDVI images of Landsat 7 were also recovered by Dr. Miao using the same algorithm.

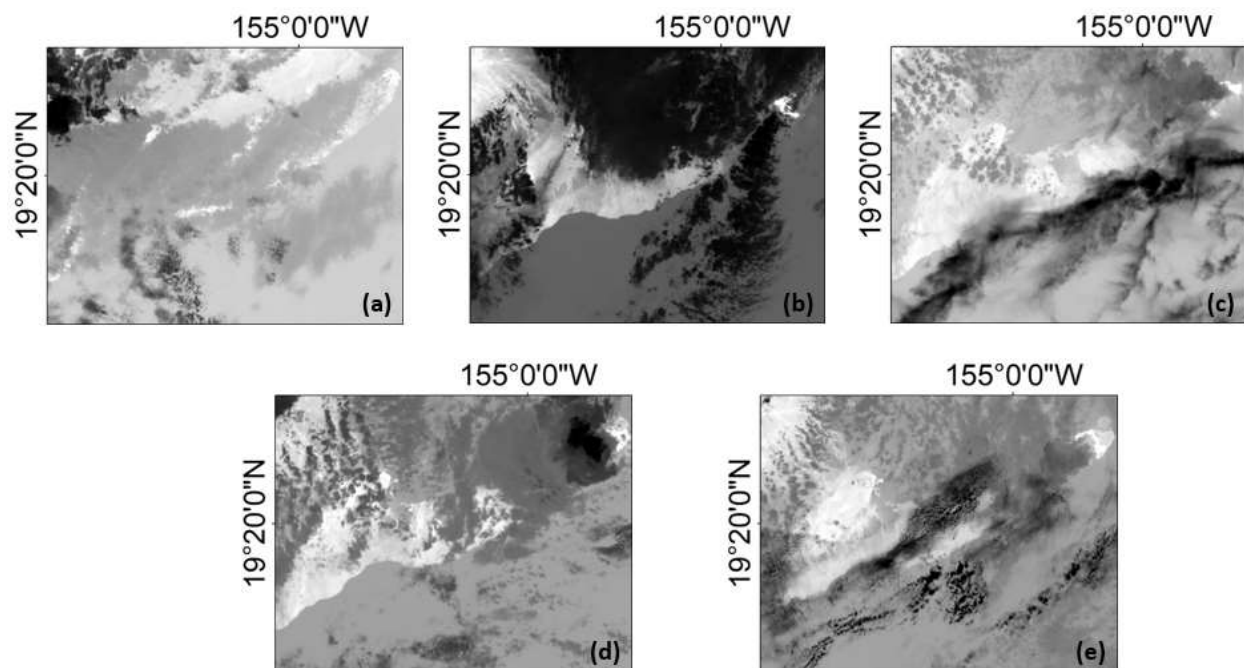


Figure 7: Images shown in Figure 6 with strips of missing data recovered by the in-painting algorithm.

I extracted the pixels with temperature greater than or equal to 50°C from all thermal images and combined them with each subsequent temperature image. Figure 8 shows the combination images of the temperatures greater than 50°C .

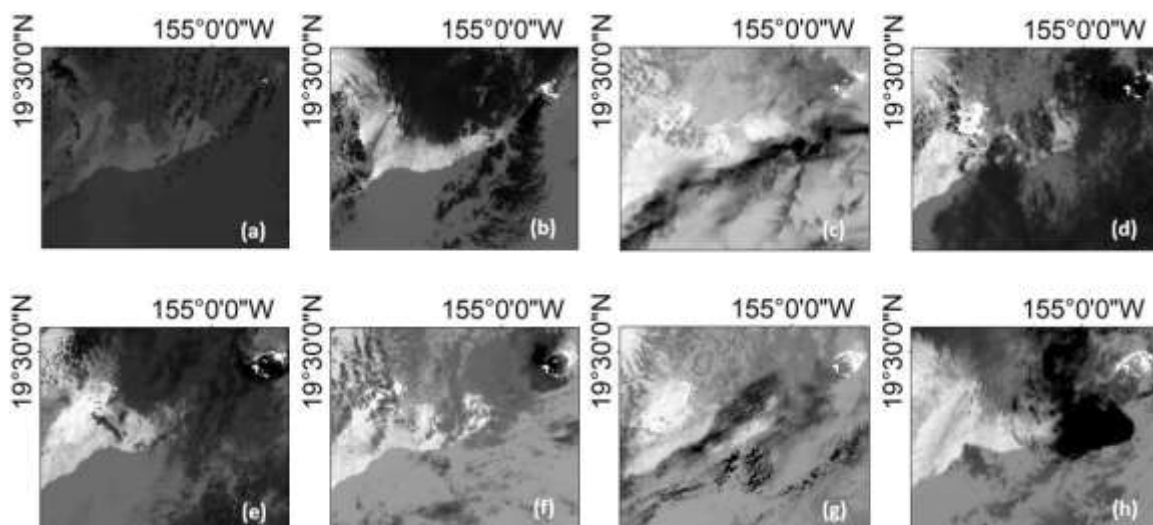


Figure 8: Combinations of temperature images generated by extracting the temperatures greater than or equal to 50°C from all the previous images. (a) Temperature image of May 14, (b) May 22, (c) June 07, (d) June 15, (e) July 01, (f), July 09, (g) July 25, (h) August 02, 2018.

3.3. Airborne LiDAR

Two airborne LiDAR surveys were conducted as a part of the Rapid Response Imagery Products (RRIP) of the United States Geological Survey (USGS) to monitor the volcanic activity at the East Rift Zone of the Kīlauea volcano in 2018. The first LiDAR survey was conducted by Quantum Spatial Inc. between June 1 and 15, 2018. An area of approximately 105 km² was surveyed over 2 weeks and 11 flights. The LiDAR data was processed by the U.S. Army Corps of Engineers' (USACE) Geospatial Repository and Data Management system (GRiD) (<https://perma.cc/8R4X-Q96W>). The second survey was conducted in a collaboration among U.S. Army Cold Regions Research & Engineering Lab (CRREL), University of Houston, and USGS between July 8 and 12, 2018 (<https://Kilauealidar.com/>), during which an area of approximately 122.4 km² was mapped over 9 flights. The spatial resolution of the LiDAR data was 0.5 m. The areas of the two LiDAR surveys do not overlap exactly; data of the first survey covers a small portion of the Vacation Island and excludes the Halema'uma'u crater, while the data from the second survey covers the whole Vacation Island and the Halema'uma'u crater. USGS (2018a; 2018b) offers the vertical differencing from the two overlapping data sets. Figure 9 shows the difference in the acquisitions of both LIDAR surveys.

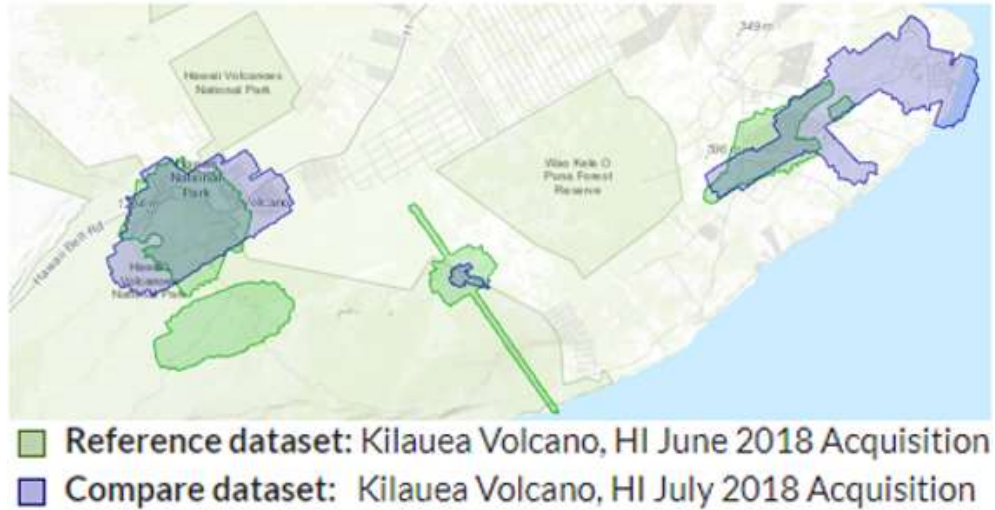


Figure 9: Map showing the difference in acquisition areas from both LiDAR surveys

I compared the InSAR and LiDAR datasets over the Pu'u O O crater and the surrounding area, where coherence from the InSAR images was high due to the absence of vegetation. Pu'u O O is a volcanic cone in the East Rift Zone of the Kīlauea volcano. Location of the Pu'u O O crater and the differenced LiDAR imagery over the crater can be seen in Figure 10. Since the dates of the two LiDAR data collections vary from June 1 to June 15, 2018 and from July 7 to July 12, 2018, respectively, I generated a separate interferogram between June 7 and July 13, 2018, and determined the vertical displacement. Then I compared the results from LiDAR and InSAR to determine the difference between the data sets generated by the two different remote sensing techniques.

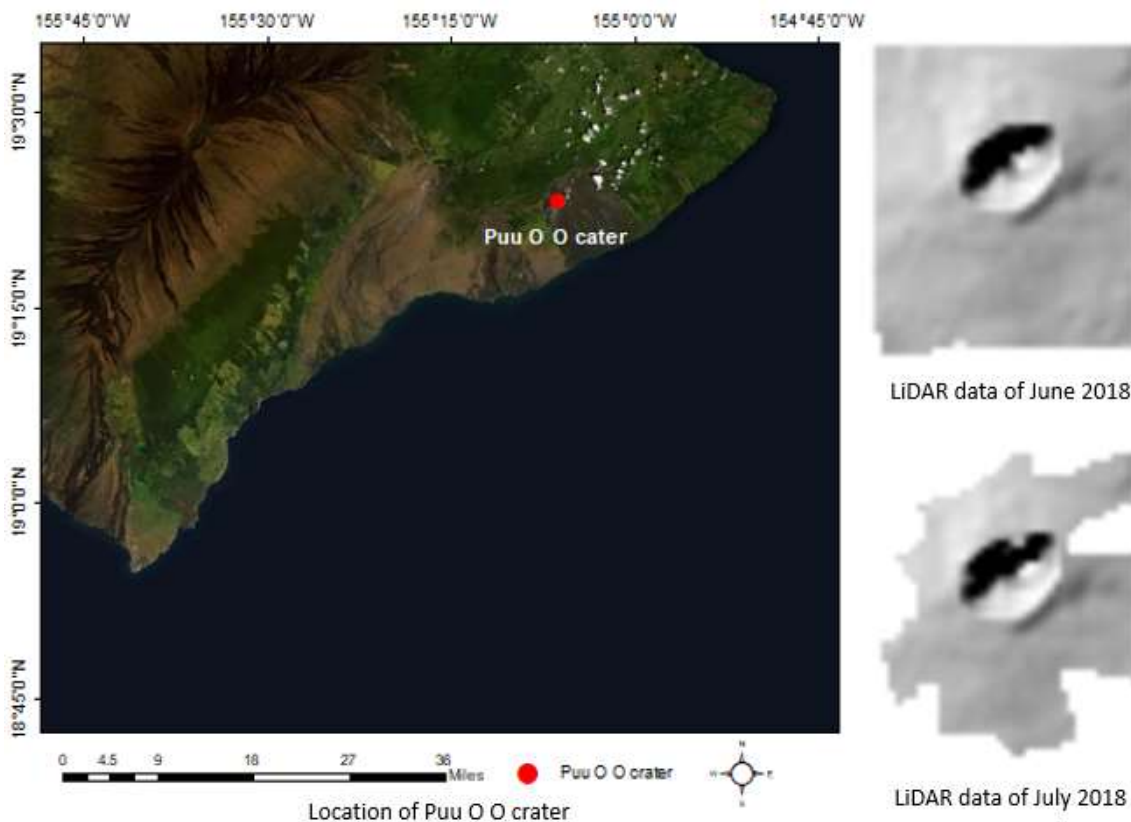


Figure 10: Images showing location map of Puu’O’O crater and LiDAR data at the crater. Image resolution is set at 30m. LiDAR image courtesy: <https://opentopography.org/>

3.4. Other Accessory Data

Other data used in this study was downloaded from the National Aeronautics and Space Administration’s (NASA) Fire Information for Resource & Management System (FIRMS). NASA’s FIRMS is a program that distributes the global hotspot data. The data is distributed in three different categories: Standard Processing (SP), Near Real-Time (NRT) processing, and combination of both. The NRT data is available within 3 hours of detection but is only available to public temporarily, while the SP data is publicly archived (<https://firms.modaps.eosdis.nasa.gov/>). FIRMS data is collected by two sensors: MODIS and Visible Infrared Imaging Radiometer Suite (VIIRS). The data from FIRMS is pre-processed and displayed in 4 levels; Level 0 is a presumed forest fire, level 1 is considered an active volcano,

level 2 is for other stationary ground sources, and level 3 is for offshore sources (Schroeder et al., 2014). I used the VIIRS data to make a point that some discrepancy in the Landsat and VIIRS data was present, since Landsat 7 and Landsat 8 thermal images by themselves could not distinguish between lava and forest fires caused by lava. Figure 11 shows the hotspots detected by VIIRS and Landsat 8.

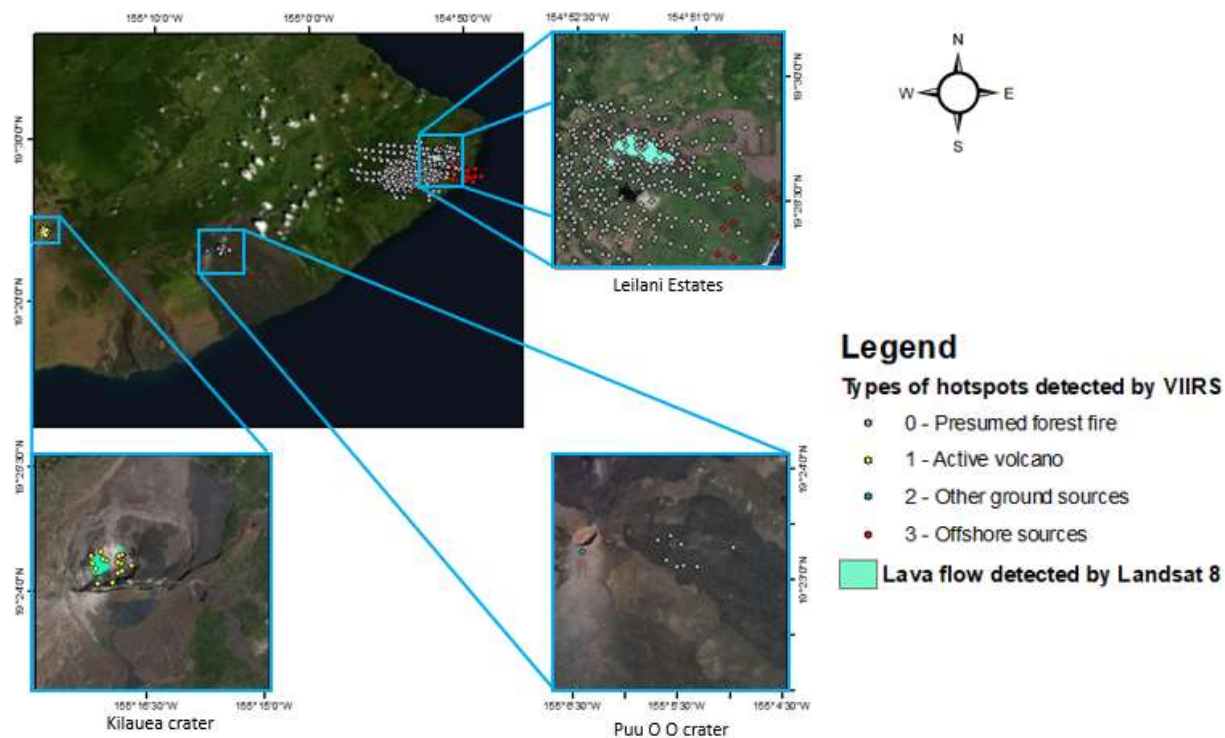


Figure 11: Map showing distribution of hot spots detected by VIIRS and Landsat 8 over the Kilauea crater and East Rift Zone. The VIIRS data were acquired between May 13 and May 19, 2018, and the Landsat 8 image was acquired on May 14, 2018.

4. Algorithm for Estimating the Area and Volume of Lava

I developed an algorithm to estimate the aerial coverage and volume of lava by removing the deformation due to geothermal sources and forest fires. Figure 12 shows the flowchart for the algorithm I developed for estimating the areal coverage and volume of lava erupted recently.

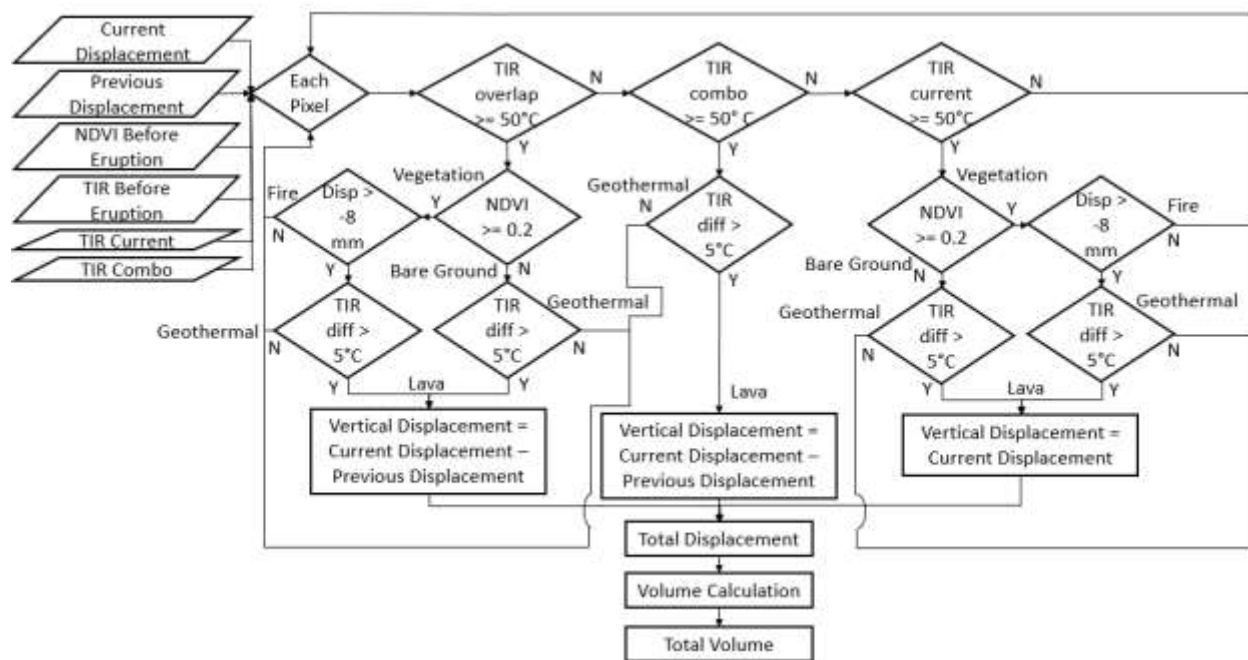


Figure 12: Flowchart of the procedure for estimating lava area and volume erupted.

For the process, the inputs required are the displacement images derived from InSAR processing for both current and previous dates, temperature images before and after the eruption, combination image generated from all temperature images (temperature greater than 50°C) for all previous acquisitions, and the NDVI image before the eruption. The significance of each input requirement is explained below.

I used the thermal images to determine the area inundated by lava based on the fact that lava has much higher temperature than the background temperature. Since the maximum detectable temperature in the Landsat 8 image is 94° C, any temperature above 94° C was set to 94° C by the product algorithm (Reuter et al., 2015). Although I was unable to obtain the actual

temperature of lava pixels from the thermal images acquired by Landsat 7 and 8, the natural land surface with temperature equal to or greater than 94° C must be either lava, land surface with geothermal resources, or fire. However, some areas inundated by lava might have temperature less than 94°C if the lava had cooled down. Therefore, I performed the sensitivity analysis to determine the threshold temperature as an input requirement. The threshold temperature would be less than 94°C, but more than the natural land surface temperature. The natural land surface temperature at Hawaii in summer is about 30°C on average (<https://perma.cc/K772-QC8M>). Therefore, considering variations in the land surface temperature, I generated a histogram for temperatures between 40°C and 94°C. Figure 13 shows the histogram of the Landsat 8 thermal image acquired on May 14, 2018 for the temperature range between 40°C and 94°C.

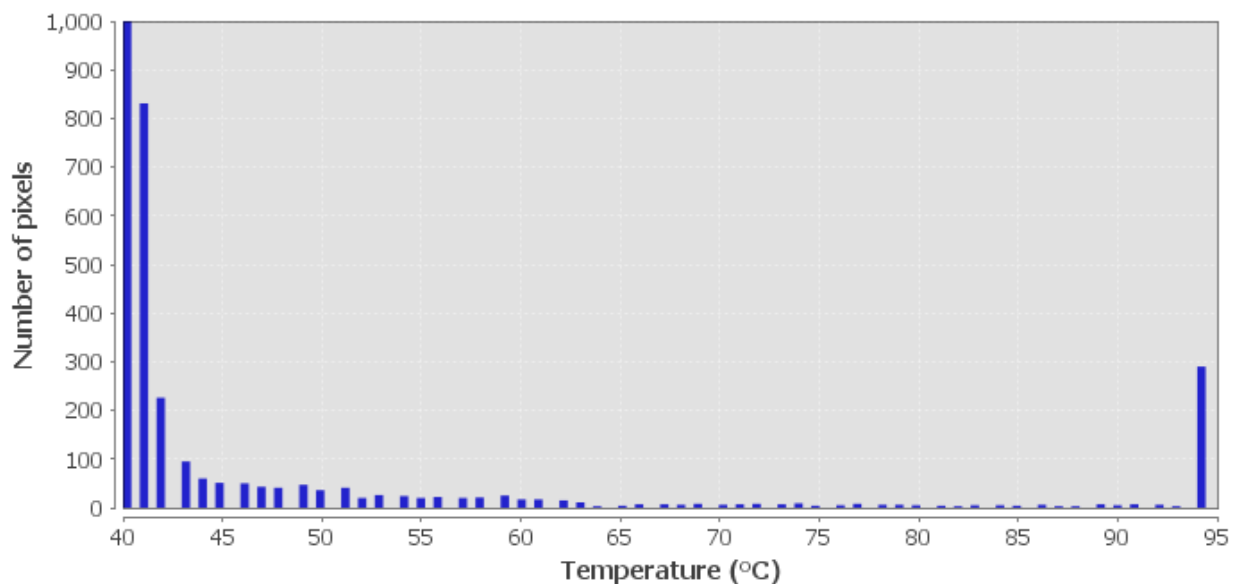


Figure 13: Histogram for the temperature sensitivity analysis between temperatures 40°C and 95°C.

Figure 13 shows that the number of pixels decreases rapidly between 40°C and 43°C, meaning that a majority of the area has a temperature below 40°C. Since air temperature in Hawaii has never been higher than 35° C (95° F) in the past record

(<https://www.usnews.com/news/best-states/articles/2019-09-27/hawaii-saw-record-breaking->

[temperatures-this-summer](#)), a land surface with temperature greater than or equal to 35° C must be due to the land surface of geothermal sources, wildfires, or recently erupted lava. Considering elevation in temperature due to the thermal anomalies, I set 50°C as the temperature threshold to separate pixels of usual land surface temperature from the pixels of anomalously high temperature that is likely caused by recently erupted lava, geothermal heat, and wildfire.

I used the NDVI images before the eruption to distinguish between lava and forest fires (vegetated areas with temperature greater than 50°C) pixels from the total anomalously hot pixels. I identified the active wildfire area using a combination of temperature and NDVI of the area before the eruption as a proxy for vegetation or forests. I extracted the pixels from the thermal image of May 14, 2018 acquired by Landsat 8 with temperature values greater than 50°C and created a shapefile, and then extracted the NDVI image of April 12, 2018 acquired by Landsat 8, using the same shapefile. Figure 14(a) shows the clipped temperature and NDVI images over the Kīlauea crater, Figure 14(b) shows the clipped temperature and NDVI image over the Leilani Estates, and Figure 14(c) shows the histogram of the clipped NDVI images over the Kīlauea crater and the Leilani Estates. Figure 14(a) shows that since the lava lake was visible at that time, the temperature was greater than 50°C. However, since no vegetation is present over the crater, NDVI was less than 0. Figure 14(b) shows that since vegetation was present before the eruption, NDVI was greater than 0.2.

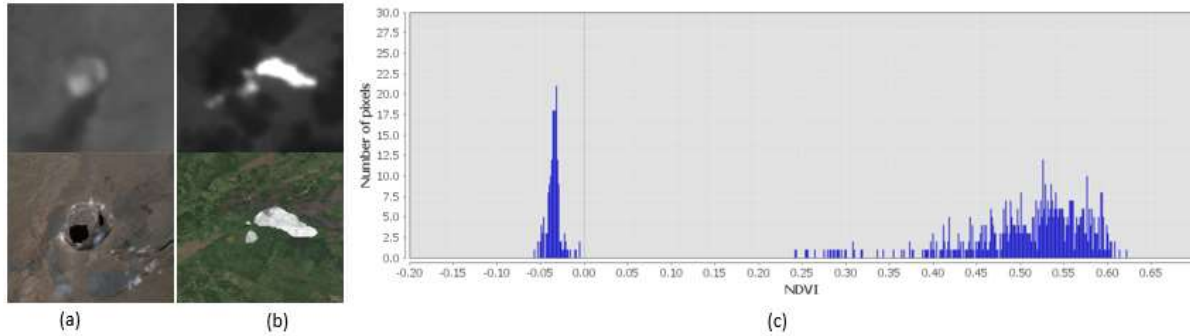


Figure 14: (a) Temperature (top panel) and NDVI (bottom panel) of the Kīlauea crater, (b) temperature (top panel) and NDVI (bottom panel) in the vegetated area in the Leilani Estates, (c) histogram of the clipped NDVI image.

From the histogram (Figure 14 (c)), I separated the vegetated areas from non-vegetated areas by setting the NDVI threshold to be 0.2. Therefore, any pixels that had the temperature above 50°C and NDVI greater than 0.2 were classified as either wildfire, or lava flowing through a vegetated area. Liu et al., (2014) showed that the InSAR derived subsidence of up to 8 cm following wildfires in the Arctic Tundra region, in which thawing of the permafrost might have played a major role in the deformation. Since tropical region of Hawaii would not encounter permafrost, subsidence due to just wildfires could be far less. However, since the lava would inundate the area and cause only the uplift and not subsidence, any pixel with the temperature greater than 50°C and the deformation less than or equal to 0 was considered as forest fire and was excluded from further analysis.

After excluding the deformation due to wildfires, the next task was to remove the area with geothermal sources, since many geothermal sites are present near the Kīlauea crater and the ERZ. To remove the area with geothermal sources and the Kīlauea crater from the total anomalously hot area, I made use of the fact that the geothermal sources near the volcano and the crater will have higher temperature than atmospheric temperature and the difference in the temperature images before and after the eruption will be almost zero, assuming that the

temperature of the geothermal area is almost constant. For that, the thermal image acquired on April 12, 2018 (before eruption) was subtracted from that acquired on May 14, 2018 (after eruption) to form a temperature difference image (Figure 15(a)).

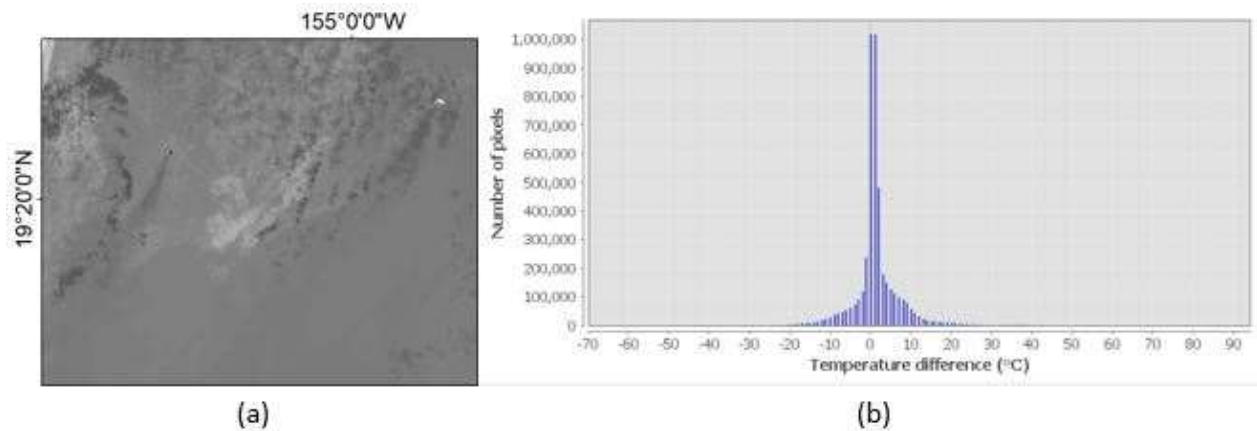


Figure 15: (a) Temperature difference image shows that the Kilauea crater and some other areas are masked and only lava has high temperature difference, (b) the histogram of the temperature difference image.

Figure 15(b) shows the histogram of the temperature difference image. More than 85% pixels in the temperature difference image had the temperature difference up to 5°C, indicating near-constant temperature in both images. I set the temperature difference of 5°C as the threshold to separate geothermal pixels from recently erupted lava pixels to guarantee all geothermal pixels are excluded from the total anomalously hot pixels. Hence, if a pixel, which was already considered to be of high temperature ($> 50^{\circ}\text{C}$) and had a NDVI value less than 0.2, it must be a geothermal pixel if the temperature difference of the pixel was less than 5°C.

The algorithm had three primary conditions for determining the presence of lava and estimating its volume. Since the master image for forming the interferograms was the same, once the lava had inundated the land, the deformation will be present in all the subsequent interferograms. Also, some pixels from the temperature image of the current date were observed to be overlapping the pixels of the combination image of all the previous temperature images.

Therefore, the first condition was to see if the selected pixel of higher temperature was overlapping the same pixel of earlier temperature images or not. If it was, then to avoid the over-calculation of the displacement, the displacement value of that pixel from the previous date was subtracted from that of the current date, since that displacement was already calculated in analyzing the image of previous date. If the lava was detected in previous temperature image but not in current image, then it must have cooled down. Still, displacement while the lava was cooling down was possible, so the displacement value of that pixel of previous date was again subtracted from the current date. But since this pixel was not detected in the temperature image of the current date, it was surely not fire. Therefore, the condition to check for the wildfires was exempted in this case. A third possibility was newly erupted lava (not detected in any previous temperature images), and all the conditions were applied to the pixels falling under this category. The displacement values of these pixels were taken in their entirety.

I repeated the above procedure for each pair of Sentinel-1A images, a Landsat thermal image and Landsat NDVI image. Pairs of such imagery used are listed in Figure 16, where each double arrow sign indicates a pair.

Landsat 7	Sentinel 1-A	Landsat 8
April 04	April 20	April 28
May 22	May 02	May 14
	May 14	
June 07	May 26	May 30
	June 07	
June 23	June 19	June 15
	July 01	July 01
July 9	July 13	July 17
July 25	July 25	
	August 06	August 02
August 10	August 18	August 18

Figure 16: Sentinel-1A SAR images and Landsat 7 and 8 temperature and NDVI images used to estimate the volume of lava erupted. A double-arrow sign indicates a pair of images formed by a displacement image derived from SAR image and a thermal and NDVI images derived from Landsat 7 and 8 used together for lava volume estimation.

The procedure to estimate the lava areal coverage and volume calculation required a combination of SAR, thermal infrared, and NDVI images, as discussed above. Since thermal infrared and NDVI images were derived from the same Landsat 7 & 8 data packages, both of them are referred together as Landsat imagery. I selected the image pairs for analysis as follows: data acquired by different satellites but on the same days would provide the best estimate of lava area and volume. Both Landsat 7 and Landsat 8 acquired the image over Hawaii on the same day as Sentinel-1A at every 48th day. Therefore, for the time span of 3 months covered in this study, two Landsat 7 and two Landsat 8 images were acquired on the same days as Sentinel-1A. So, four pairs had the least time gap possible. Four other pairs were also created, where the thermal image was captured 4 days before a SAR image. The eruption ended on August 4, but hot lava was still flowing towards the Pacific Ocean, as detected by the temperature image of Landsat 7 acquired on August 10, 2018. However, since the land areas in the Landsat images of August 10 and August 18, 2018 both were almost covered by clouds, these images were not utilized.

Therefore, the temperature image combination of August 2 was combined with the SAR image of August 18 instead. In total, I generated and analyzed nine pairs of images.

5. Results

5.1. Estimated Area and Volume of Erupted Lava

I applied the algorithm developed in Section 4 to the eruption of the Kīlauea volcano in 2018 as a case study. The total volume of erupted lava was estimated to be $3.31 \times 10^7 \text{ m}^3$. The volume of the erupted lava evolved over time. Therefore, the estimated volume at the 11th day (May 14) of the first eruption was in the order of 10^4 m^3 . Massive eruption and lava flow had taken place on May 27 and 28, 2018. Therefore, the erupted volume increased afterwards, and since June 07, the volume of the lava was in the order of 10^5 m^3 or more. Total area inundated by the lava was estimated to be 12.68 km^2 , including the new land added to the Big Island. Total vegetated area destroyed during the eruption was found to be 12.32 km^2 . Figure 17(a) shows the total area on the ERZ inundated by lava and the Figure 17(b) shows the vegetation destroyed in the eruption event, as detected by the algorithm developed in this study.

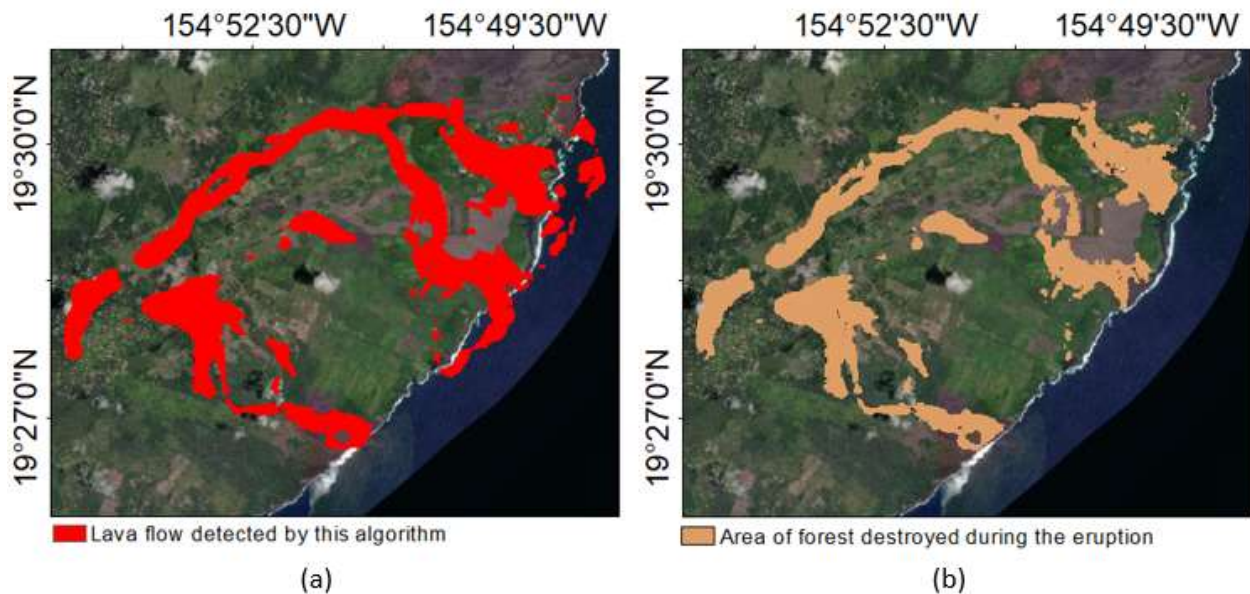


Figure 17: (a) Land area inundated by lava (in red) detected by my algorithm between May and August, 2018, (b) Vegetation destroyed in the eruption episode.

5.2. Comparison between Vertical Displacements Derived from InSAR and LiDAR Analysis

Using the vertical displacement derived from LiDAR as reference, I calculated the absolute and relative difference between the InSAR derived vertical displacement and that derived from LiDAR over the Pu'u O O crater. I first define in Equation (1) the absolute difference and in Equation (2) the relative difference between the LiDAR and InSAR displacement images over the same area as:

$$\text{Absolute difference} = \text{LiDAR} - \text{InSAR} \quad (1)$$

$$\text{Relative difference} = \frac{\text{LiDAR} - \text{InSAR}}{\text{LiDAR}} \times 100 \quad (2)$$

Figure 18 shows the vertical difference image derived from the LiDAR data, vertical displacement derived from the InSAR processing and absolute and relative difference images derived using Equations 1 and 2, respectively.

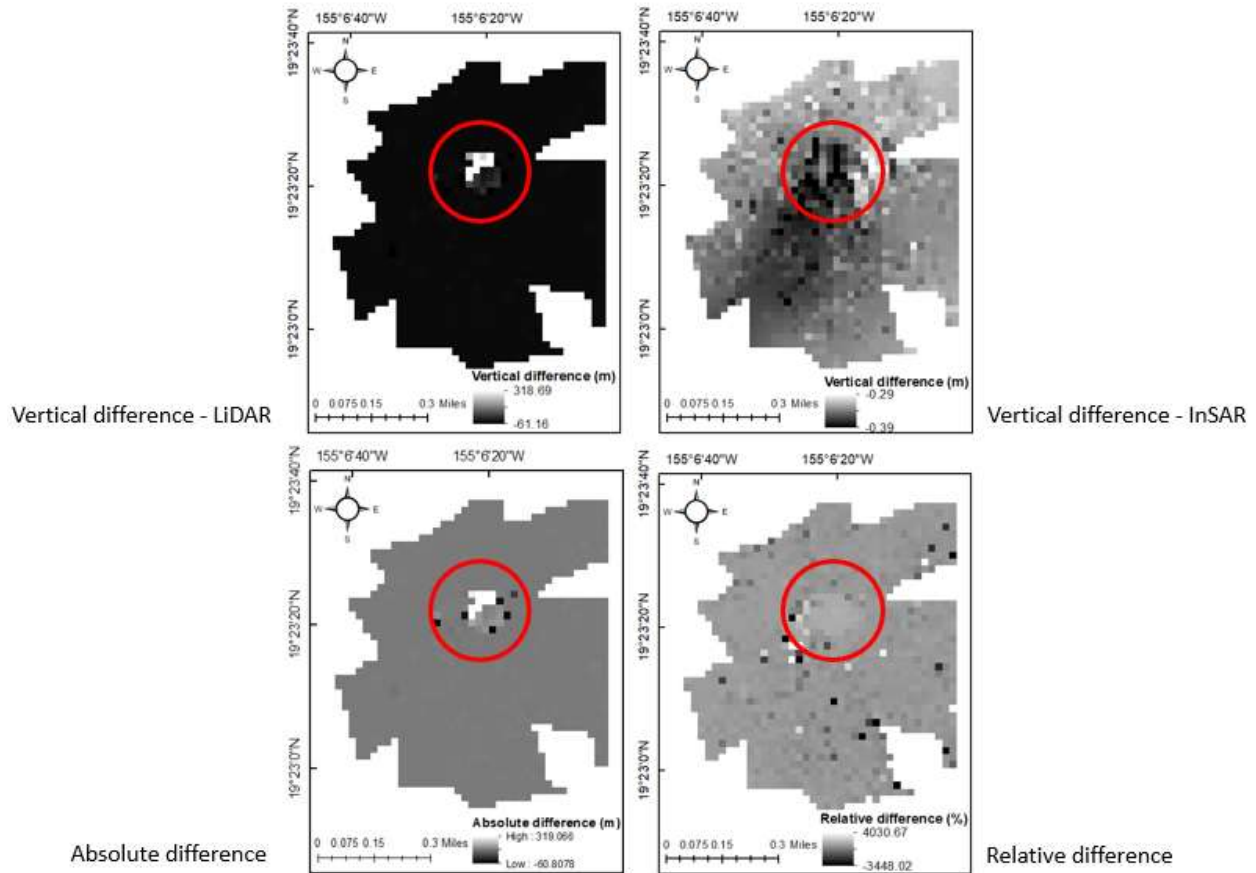


Figure 18: Images showing the vertical difference derived from the LiDAR data between June and July 2018 (Left top), the vertical displacement image derived from InSAR between June 7 and July 13, 2018 (Right top), absolute difference image between InSAR and LiDAR data (Left bottom) and relative difference image between InSAR and LiDAR data (Right bottom). The red circle in all images mark the area inside the Pu'u O O crater.

Figure 19 shows the histogram of the relative difference image of the vertical displacement derived from the InSAR and LiDAR data. We can see the rapid decline in the number of pixels with increasing relative difference in both positive and negative directions.

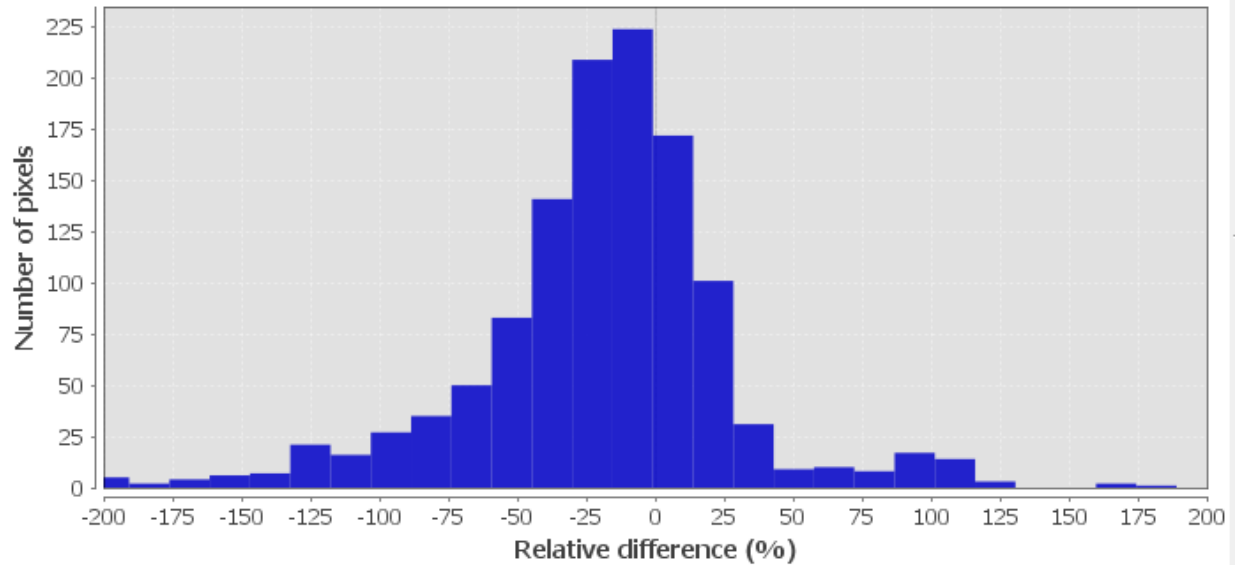


Figure 19: Histogram showing the relative difference between vertical displacement calculated by InSAR and LiDAR. Pixels with high percent difference are inside the Pu'u O O crater.

I performed the sensitivity analysis by taking the absolute values from the relative difference image. Figure 20 shows the graph generated after sensitivity analysis. From Figure 20, we can see that 12.42% pixels had a relative difference less than 5%, 24.36% pixels had an absolute relative difference less than 10%, and likewise, more than 50% pixels had an absolute relative difference less than 30%. Overall, 72.37% pixels had an absolute relative difference less than 50%. 347 out of 1256 pixels had a relative difference greater than 50%. Analysis of the absolute difference image shows that 1216 out of 1256 pixels had an absolute difference less than 1m. This indicates a good correlation between the InSAR and LiDAR derived vertical displacements.

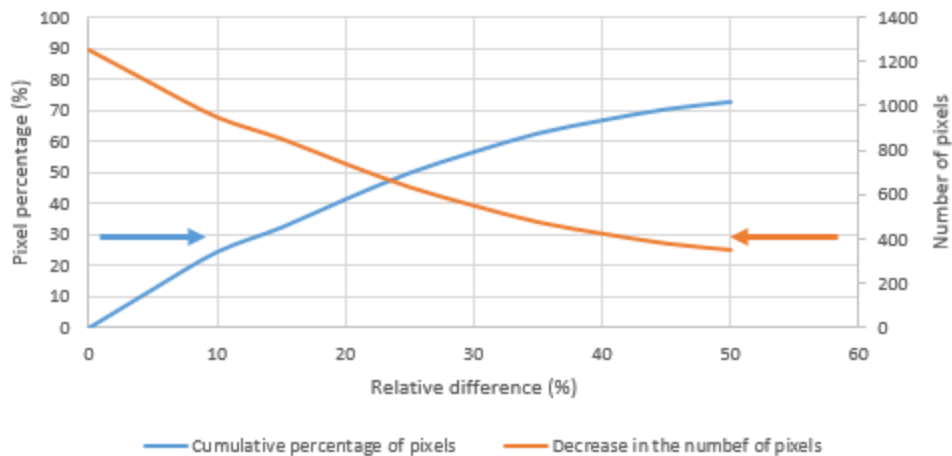


Figure 20: Graph showing the results of sensitivity analysis performed on the relative difference image between InSAR and LiDAR acquisitions. Yellow line represents the decline in the pixels with increasing relative difference, blue line represents the cumulative percentage of pixels with relative difference.

5.3. PSI Analysis

The PSI method was implemented to the 17 Sentinel-1A interferometric SAR images acquired in the ascending node between March 3 and September 23, 2018. Figure 21 shows the area covered in our study and velocity map generated by the StaMPS algorithm.

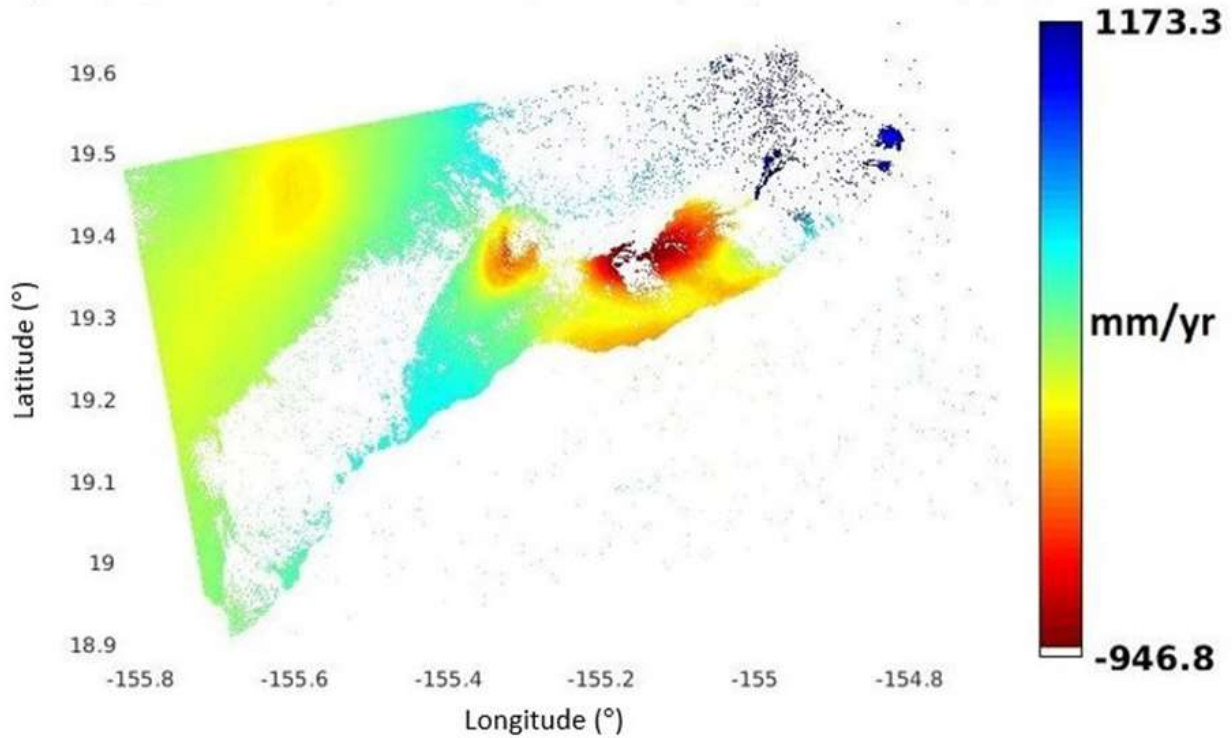


Figure 21: Velocity map showing the area covered in my study.

16 unwrapped interferometric maps were generated using the StaMPS algorithm explained in the Methodology section. The unwrapped phase refers to the phase difference due to the relative motion of the ground target with reference to the radar in slant range coordinates over the timeline. For the interferometric pairs of March 03, March 15, March 27 and April 8, since the master post-dated the slave, positive value indicates the movement towards the satellite, while the negative movement indicates the movement away from satellite. For the rest of the images, positive phase indicates the movement away from the satellite and the negative phase indicates the movement towards the satellite. All the unwrapped interferograms show the phase difference due to the displacement of ground targets with reference to the master image of April 20, 2018. Wrapped and unwrapped interferograms are shown in Figure 22 and Figure 23, respectively.

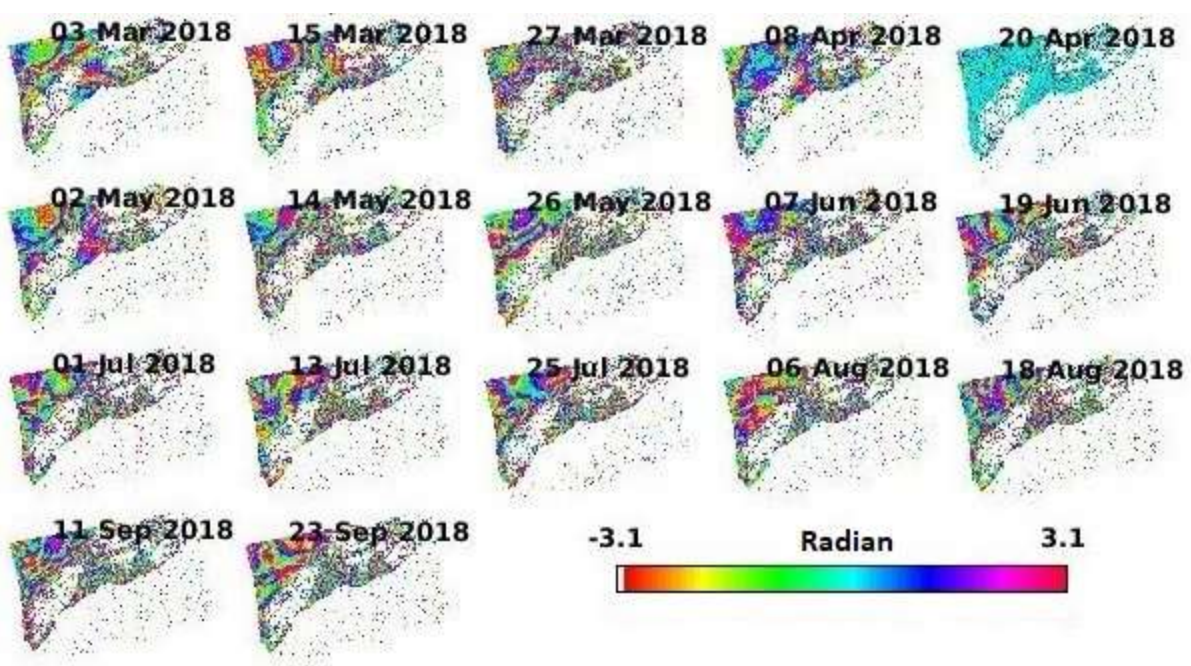


Figure 22: Wrapped interferograms generated by StaMPS tool.

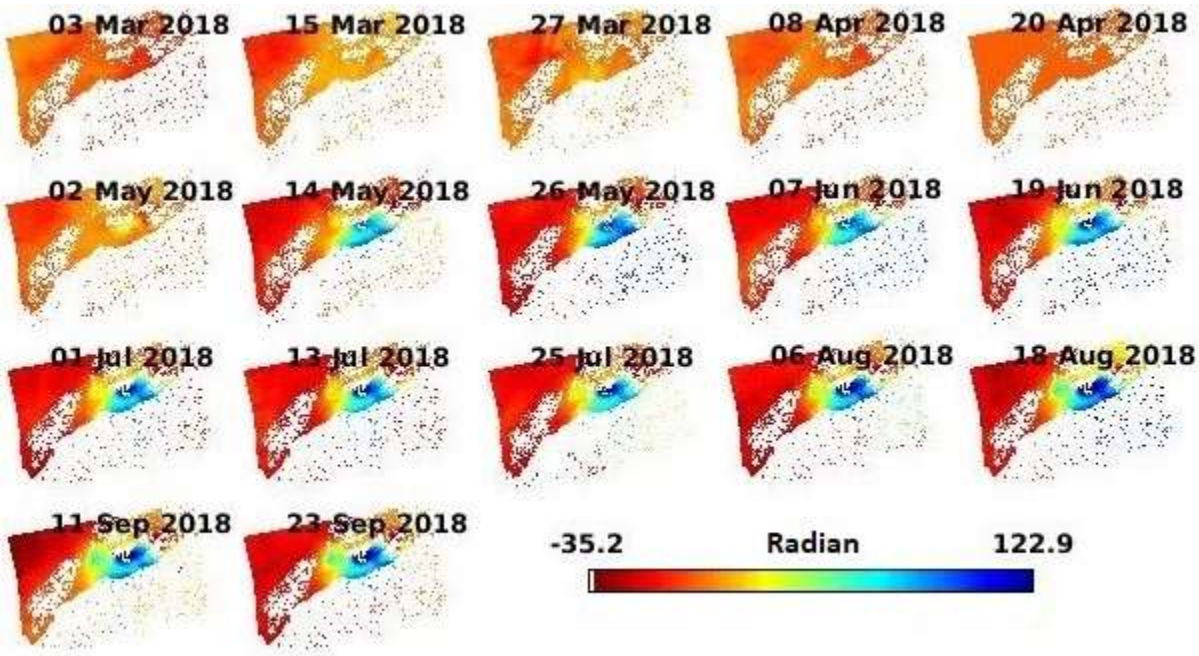


Figure 23: Interferograms generated after phase unwrapping.

Figure 22 shows that the interferometric fringes are closer to each other at Kīlauea crater and the ERZ, indicating displacement. Figure 23 shows that after phase unwrapping, the phase

difference between two SAR images is high at the ERZ, but not on the Mauna Loa. Figure 23 also shows that while the Big Island was active even before the eruption, activity was minor. However, since May 02, large deformations can be seen at and near the Puu'O'O crater, which is due to the collapse of the Puu'O'O crater on April 30, 2018 (Neal et al., 2019).

To analyze the evolution of deformation and determine the regional correlation in topographic displacement related to the eruption, I performed a time-series analysis at various key locations throughout the region, from Mauna Loa to the eastern tip of the island. Figure 24 shows the locations of the points selected for time-series. Figure 25 shows the time-series plots generated for each selected point.

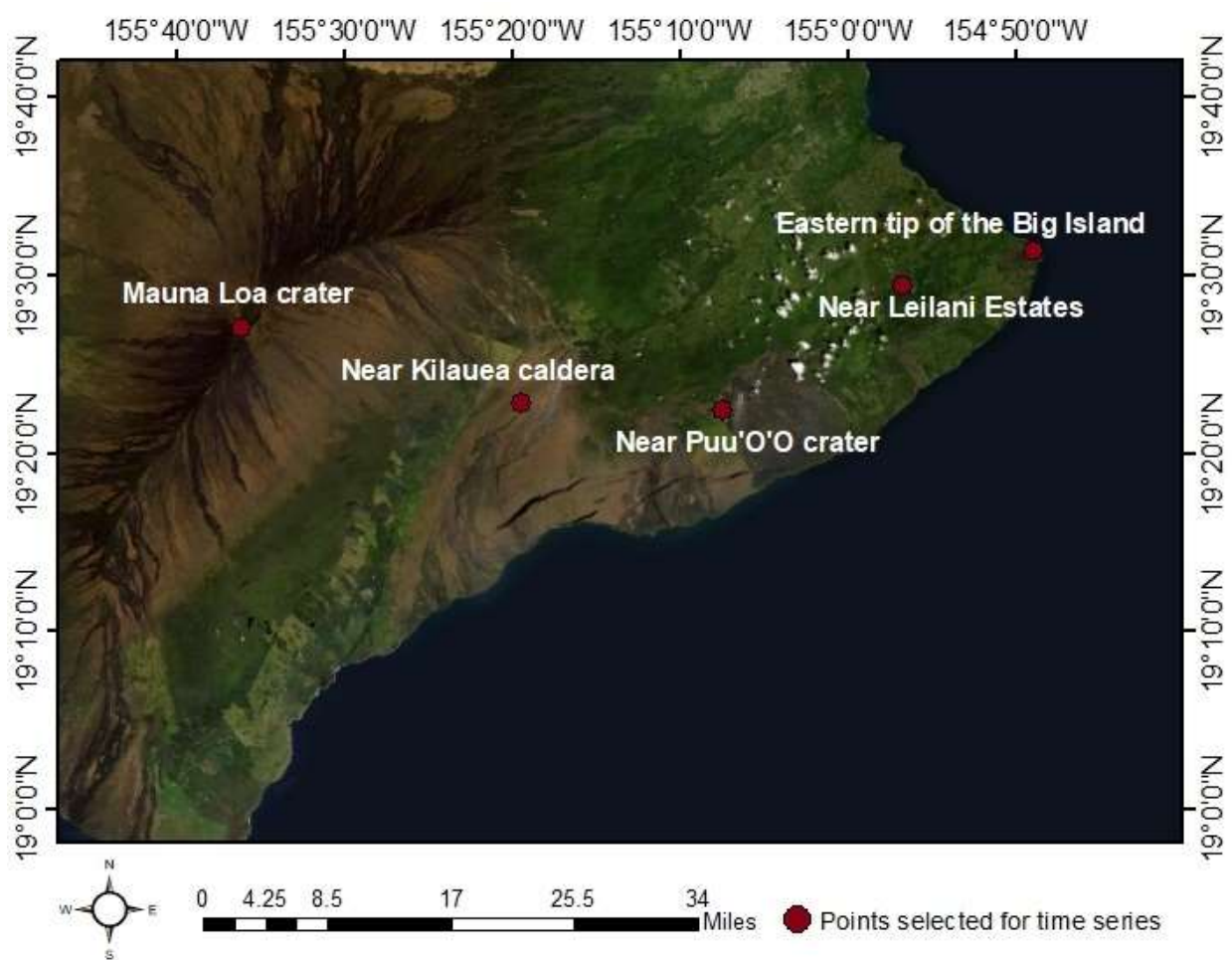


Figure 24: Locations of the points selected for time series.

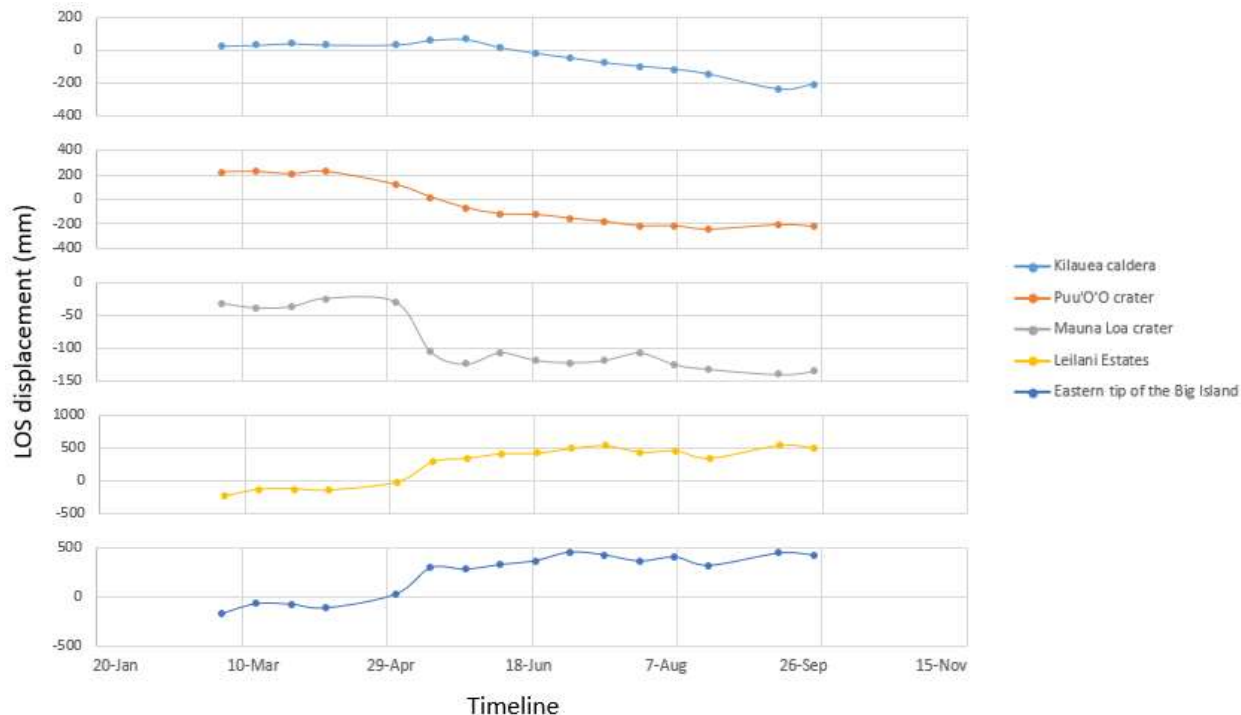


Figure 25: Time series plots of the selected points.

Figure 25 shows that all the time-series plots show nominal displacement before May 02, 2018. After May 02, the point on the Puu’O’O crater starts to subside rapidly, following the collapse of the Puu’O’O crater. The subsidence continues up to September, where a sudden uplift can be seen, followed by further subsidence. The similar trends can be seen in the time series of a points near the Kīlauea caldera and Mauna Loa crater. Time series plots of the Leilani Estates and the eastern tip of the island, however, tell a different story. Both the areas (Yellow and Dark Blue plots in Figure 25) show the uplifting of the region during the eruption, indicating the intrusion of magma beneath them and/or inundation of lava over them. Therefore, the southern and south-western parts of the Big Island seem to be subsided during the eruption at the eastern side, indicating the deflation of the island due to the loss of internal pressure. The time-series

plots of Kilauea (Light Blue), Puu'O'O crater (Orange), Mauna Loa (Gray) have a good correlation between each other.

6. Discussion

6.1. Estimated Area and Volume of Erupted Lava

The total volume of lava erupted was estimated to be $3.31 \times 10^7 \text{ m}^3$ between May and August 2018 using the Sentinel-1A InSAR and Landsat 7 & 8 thermal & NDVI image based multiple remote sensing techniques. Lundgren et al. (2019) estimated the subaerial lava flow volume be approximately $5.93 \times 10^8 \text{ m}^3$. Therefore, the estimate derived by my algorithm solely from the satellite data is less than that estimated by Lundgren et al. (2019). The algorithm we developed used the space-borne Landsat 7 and 8 thermal images to isolate the pixels with lava. Therefore, what my algorithm estimated was basically the hot lava detected by the thermal sensors during the eruption. If the summit collapse of 2018 drove magma toward the ERZ as suggested by the ERZ pressure pulses (Neal et al., 2019), substantial magma drainage from magma storage beneath the former east margin of the Halema'uma'u crater would have occurred and part of the lava would have filled up the deeper magma storage beneath the south part of the caldera considering a well-connected magmatic plumbing system from the volcano's summit to its lower flank (Babu & Kumar, 2019). The magma driven to the rift zone would be either as intrusion dikes, or vigorous lava effusion and degassing.

The estimate generated by my algorithm did not include the lava that flowed into ocean since InSAR analysis was only performed over the land surface. For instance, on 18 May, 2018, long and fast-moving lava erupted from the LERZ fissures reached the ocean on the southeast side of the island on May 23, 2018. Lava re-erupted in east-central Leilani Estates from late May 27 to May 28, 2018 and fed a rapid channelized flow that ultimately entered the ocean near the eastern tip of the island (Neal et al., 2019). The volume of the lava lost into ocean and the lava that created approximately 3.78 km^2 of new land at the eastern tip of the Big Island (Babu &

Kumar, 2019) could not be estimated by the InSAR-based technology due to unavailability of coherent pixels in the master SAR image of April 20, 2018. Thickness of the lava from the new land was on average 20 m (Lundgren et al., 2019). From the bathymetric surveys, the volume of the lava that accumulated over the continental shelf and created the new land was found to be $\sim 1.2 \times 10^8 \text{ m}^3$ (Lundgren et al., 2019). Figure 26 shows the added area in the Big Island due to cooling and solidification of lava in Pacific Ocean.

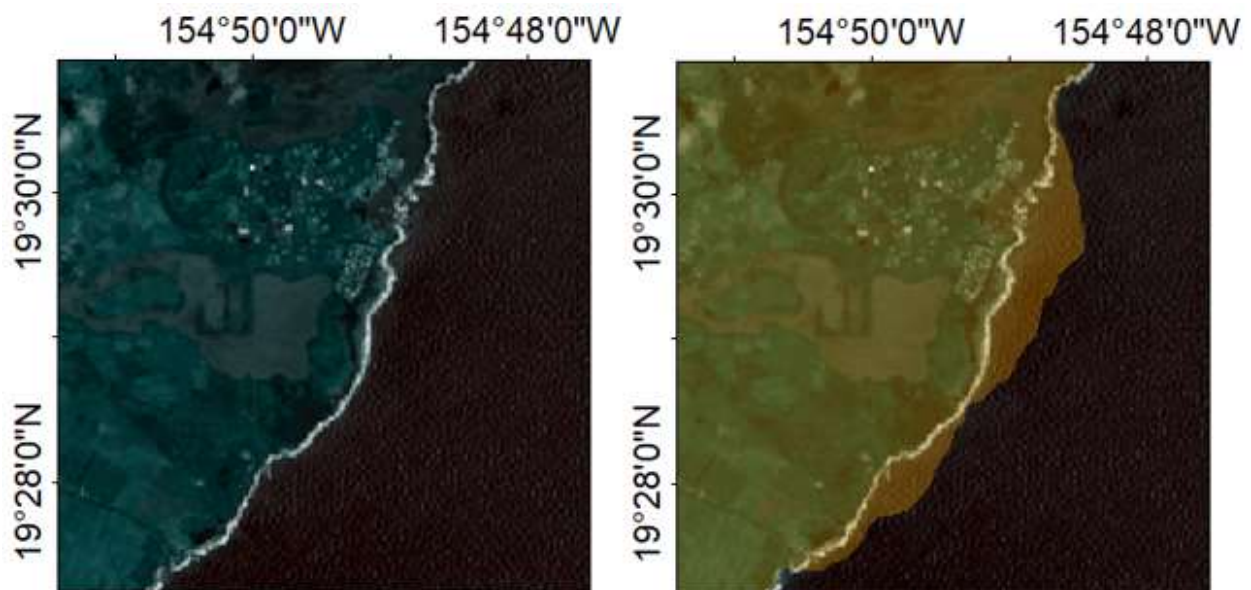


Figure 26: Landsat 8 image of April 12, 2018 (Left) and Landsat image of April 12, 2018 superimposed by the shapefile created from the Landsat 8 image of September 19, 2018 (Right) showing the addition of new land due to cooling and solidifying of the erupted lava in the ocean. Shapefile was created visually.

Babu and Kumar (2019) mentioned that the Puu'O'O crater had collapsed due to the withdrawal of magma, caused by pressure imbalance in the magma conduit beneath it, resulting in the opening of new pathways for magma to be diverted to the Leilani Estates. They also mentioned that because the Kīlauea's summit caldera and Puu'O'O crater share the same magma plumbing system, a pressure imbalance beneath the Puu'O'O crater resulted in the magma withdrawal from summit caldera as well, ultimately resulting in the collapse of the Halema'uma'u crater in following days. The eruption stopped suddenly in August, 2018, which

could be due to the magma conduits supplying the magma to the fissures being blocked, ceasing the magma flow. This could be due to the rift movement, as explained in Babu and Kumar (2019). Due to the sudden block in the flow, some amount of lava drained from the summit caldera and replenished from the magma chamber might have been stuck and solidified inside the conduit itself beneath the fissures, preventing anymore effusions on the surface. The volume of the magma withdrawn from the summit caldera that redirected to the eastern part but solidified underground, or intruded as dykes could not be detected or estimated by our algorithm, if the surface temperature was less than 50°C. Lava erupted and cooled down between two Landsat acquisitions could also not be estimated for the same reason.

The following factors may also impact the estimation of the volume of lava. Sentinel-1A acquires the imagery over Hawaii's Big Island from 04:30:16 to 04:30:44 GMT, Landsat 7 and 8 both acquire the imagery approximately at 20:41:50 GMT. Therefore, four of my data combinations had a temporal gap of approximately 16 hours and the other four combinations had a temporal gap of approximately 3 days and 10 hours during which, the eruption is likely to have continued. Therefore, the areas determined from the thermal images may not exactly fit the deformation images. Hence, some pixels from the displacement images might have been ignored by the algorithm. In addition, due to the lava, fire, and atmospheric conditions, the acquired Landsat images had the smoke and cloud cover up to 50%. Therefore, many pixels in the lava inundated area were covered by smoke and clouds. These pixels were also excluded by our algorithm. The development of smoke and cloud clearing algorithms would improve the area and volume estimate.

The algorithm I developed to estimate the areal coverage and volume of lava needs only the data from space-borne instruments, is cost effective, and does not require much computing

power or time. Therefore, the algorithm can be very useful in monitoring remote volcanoes and the volcanoes where in-situ and air-borne measurements are not feasible. The estimate can be further improved by removing the displacement due to atmospheric phase. Utilizing data from L or longer wavelength band SAR systems (ALOS, NISAR) for analysis would give better results, since decorrelation due to vegetation is far less in L band.

6.2. Comparison Between InSAR and LiDAR

The relative difference between LiDAR and InSAR deformation measurements (refer to Figure 19) shows rapid decline in the number of pixels with increase in relative difference. 96% pixels show an absolute difference less than 1m. Therefore, the overall results from InSAR and LiDAR agreed well between each other. Figure 18 shows that the pixels with absolute difference greater than 1m and the relative difference greater than 50 % lie mainly inside the Pu'u O O crater. Vertical differencing from LiDAR data detected an inflation within the Pu'u O O crater between June and July 2018, but InSAR could not because of coherence loss between the interferometric image pair. Therefore, sudden displacement seems to cause coherence loss and ultimately results in incorrect displacement values.

6.3. LOS Displacement

The Puu'O'O crater of the Kīlauea volcano has been active and erupting pāhoehoe lava flows since 1983 until April 30, up to its collapse. The last lava flow from the Puu'O'O crater took place on May 24, 2016, during the episode 61g

https://volcanoes.usgs.gov/volcanoes/kilauea/geo_hist_1983.html#:~:text=1983%20%E2%80%93%202018%20Pu'u%20%C5%8C'%C5%8D%20Eruption&text=By%20the%20end%20the%2

[eruption, and to the Kilauea's southeastern shore.](#)). Since the lava lake in the Halema'uma'u crater was clearly visible for almost a decade (Babb et al., 2017), the magma in the crater must be constantly replenished from its shallow magma plumbing system. Since Kilauea volcano is formed due to hotspot volcanism, the magma must be coming from deep within the Earth's mantle. Therefore, continuous replenishment of magma is logical and likely. Also, inflation of the area around the crater before any eruption due to the magma buildup, and deflation during and after the eruption due to degassing is also likely. The displacement time-series plot at the Kilauea caldera shows that the displacement was very small up to May 26, 2018 and then, subsidence is observed constantly for the rest of the timeline. The Halema'uma'u crater had collapsed in late May, so this negative displacement makes sense. The displacement time-series plot at the Mauna Loa crater shows that the point had been subsiding even before the eruption, but after May 14, the subsidence activity increased. Even though the Kilauea and the Mauna Loa both have different magma plumbing systems (Babu and Kumar, 2019), geophysical studies show that both the volcanoes might be coupled together at the asthenospheric level (Shirzaei et al., 2013b). The relationship between both the volcanoes is complicated, however. The deformation patterns over both volcanoes are sometimes similar, and sometimes they are adverse. Both volcanoes are showing the similar deformation patterns since 2005; if the inflation is detected at the Kilauea caldera, similar inflation is also detected at the Mauna Loa caldera, and vice versa. Therefore, the similar trends in the time-series derived by my PSI analysis could be the continuation of the same deformation pattern and coupling mechanism. Also, since the both volcanoes are coupled together at the asthenospheric level, they must be sharing a primary magma reservoir. Assuming this is the case, I can safely say from the PSI analysis that while the ERZ of the Kilauea volcano was experiencing the lava effusions, magma was withdrawn

from the summit caldera (Babu and Kumar, 20189; Neal et al., 2019) and was also being replenished from the primary reservoir. Therefore, when the pressure in the primary reservoir decreased due to the magma being diverted to the Kilauea's plumbing system, some amount of magma could have been diverted from the Mauna Loa's plumbing system to balance the pressure in the reservoir. Therefore, deflation could have taken place over the Mauna Loa crater. In other words, the eruption from the Kilauea's magma plumbing system seems to have caused an impact on the Mauna Loa volcano as well. Points near the Leilani Estates and at the eastern tip of the island show a gradual uplift over time. These areas show the positive displacements after May 02, which could be due to the intrusion of the dyke that fueled the 2018 eruption (Neal et al., 2019), or the subaerial lava effusions over the area. Also, the results seem to become non-linear, which could be due to the loss of coherence caused by the point being inundated by lava.

7. Conclusions

The 2018 eruption of the Kīlauea volcano is one of the first few eruptions to be monitored by advanced in-situ, airborne and space-borne instruments and modelling. The eruption has opened various new dimensions of research in volcanology, seismology and remote sensing, with multiple opportunities to study the dynamic behaviors of the volcanoes.

In this study, I developed a generalized and cost-effective algorithm to estimate the areal coverage and volume of hot lava by integrating multiple satellite based remote sensing techniques including space-borne InSAR, thermal infrared, and vegetation index techniques. I applied this algorithm to the eruption of the Kīlauea Volcano between May and August, 2018 using Sentinel-1A InSAR, Landsat 7 and 8 thermal infrared and optical images. I also compared the results from the InSAR derived vertical displacements to that obtained from LiDAR surveys. Results from InSAR and LiDAR processing were found to be very similar, except for the area inside the Puu’O’O crater, where coherence was lost, possibly due to the crater edges and sudden uplift. I estimated the areal coverage and the volume of lava. I also applied the Stanford Method of Persistent Scatterers (StaMPS-PSI) algorithm on 17 Interferometric SAR images acquired by Sentinel-1A satellite between March and September 2018, and determined the LOS displacement time-series plots for several key locations throughout the ERZ and the Mauna Loa caldera.

The following conclusions are derived from this study: (1) The algorithm generated to estimate the areal coverage and the volume of lava by integrating InSAR, thermal and optical imagery works well in monitoring the volcanic effusions, (2) the land area inundated by and volume of hot lava due to the eruption of Kīlauea Volcano between May and August, 2018 were estimated to be 12.68 km^2 and $3.31 \times 10^7 \text{ m}^3$, respectively, (3) results from InSAR and LIDAR

are very well correlatable in the areas of high coherence, and (4) the southern and western parts of the Big Island has been deflated following the eruption at the eastern side.

8. References and Bibliography

- Avdan, U., Jovanovska, G., 2016. Algorithm for Automated Mapping of Land Surface Temperature Using LANDSAT 8 Satellite Data. *Journal of Sensors*, 1480307, pp.1–8.
- Babu, A., Kumar, S., 2019. SBAS Interferometric Analysis for Volcanic Eruption of Hawaii Island. *Journal of Volcanology and Geothermal Research*, 370, pp.31–50.
- Baker, S., Amelung, F., 2012. Top-Down Inflation and Deflation at The Summit of Kīlauea Volcano, Hawai'i Observed with InSAR. *Journal of Geophysical Research*, 117(12), B12406, pp.1-14.
- Balsamo, G., Agusti-Panareda, A., Albergel, C., Arduini, G., Beljaars, A., Bidlot, J., Blyth, E., Bousserez, N., Boussetta, S., Brown, A., Buizza, R., Buontempo, C., Chevallier, F., Choulga, M., Cloke, H., Cronin, M., Dahoui, M., De Rosnay, P., Dirmeyer, P., Drusch, M., Dutra, E., Ek, M., Gentine, P., Hewitt, H., Keeley, S., Kerr, Y., Kumar, S., Lupu, C., Mahfouf, J., McNorton, J., Mecklenburg, S., Mogensen, K., Muñoz-Sabater, J., Orth, R., Rabier, F., Reichle, R., Ruston, B., Pappenberger, F., Sandu, I., Seneviratne, S., Tietsche, S., Trigo, I., Uijlenhoet, R., Wedi, N., Woolway, R., Zeng, X., 2018. Satellite and In Situ Observations for Advancing Global Earth Surface Modelling: A Review. *Remote Sensing*, 10(12), 2038, pp.1-72.
- Bekaert, D., Walters, R., Wright, T., Hooper, A., Parker, D., 2015. Statistical Comparison of InSAR Tropospheric Correction Techniques. *Remote Sensing of Environment*, 170, pp.40-47.

- Békési, E., Fokker, P., Martins, J., Limberger, J., Bonté, D., Van Wees, J., 2019. Production-Induced Subsidence at the Los Humeros Geothermal Field Inferred from PS-InSAR. *Geofluids*, 2306092, pp.1-12.
- Bonì, R., Cigna, F., Bricker, S., Meisina, C., McCormack, H. 2016. Characterisation Of Hydraulic Head Changes and Aquifer Properties in The London Basin Using Persistent Scatterer Interferometry Ground Motion Data. *Journal of Hydrology*, 540, pp.835-849.
- Chen, C., Zebker, H., 2002. Phase Unwrapping for Large SAR Interferograms: Statistical Segmentation and Generalized Network Models. *IEEE Transactions on Geoscience and Remote Sensing*, 40, pp.1709-1719.
- Chen, J., Howard A., Paul S. Asta M., 2014. The 2010 Slow Slip Event and Secular Motion at Kīlauea, Hawai'i, Inferred from TerraSAR-X InSAR Data. *Journal of Geophysical Research: Solid Earth*, 119(8), pp.6667-683.
- Chen, Y., Remy, D., Froger, J., Peltier, A., Villeneuve, N., Darrozes, J., Perfettini, H., Bonvalot, S., 2017. Long-Term Ground Displacement Observations Using InSAR And GNSS at Piton de la Fournaise Volcano Between 2009 And 2014. *Remote Sensing of Environment*, 194, pp.230–247.
- Coppola, D., Laiolo, M., Franchi, A., Massimetti, F., Cigolini, C., Lara, L., 2017. Measuring Effusion Rates of Obsidian Lava Flows by Means of Satellite Thermal Data. *Journal of Volcanology and Geothermal Research*, 347, pp.82–90.
- Crosetto, M., Monserrat, O., Cuevas-González, M., Devanthéry, N., Crippa, B., 2016. Persistent Scatterer Interferometry: A Review. *ISPRS Journal of Photogrammetry and Remote Sensing*, 115, pp.78-89.

- De Novellis, V., Castaldo, R., De Luca, C., Pepe, S., Zinno, I., Casu, F., Lanari, R., Solaro, G., 2017. Source Modelling of The 2015 Wolf Volcano (Galápagos) Eruption Inferred From Sentinel 1-A DInSAR Deformation Maps And Pre-Eruptive ENVISAT Time Series. *Journal of Volcanology and Geothermal Research*, 344, pp.246–256.
- Flood, N., 2014. Continuity of Reflectance Data Between Landsat-7 ETM+ and Landsat-8 OLI, for Both Top-Of-Atmosphere and Surface Reflectance: A Study in The Australian Landscape. *Remote Sensing*, 6(9), pp.7952-7970.
- Flynn, L., Harris, A., Wright, R., 2001. Improved Identification of Volcanic Features Using Landsat 7 ETM. *Remote Sensing of Environment*, 78, pp.180–193.
- Foumelis, M., Blasco, J., Desnos, Y., Engdahl, M., Fernández, D., Veci, L., Lu, J., Wong, C., 2018. ESA SNAP-StaMPS Integrated Processing for Sentinel-1 Persistent Scatterer Interferometry. *IGARSS 2018, 2018 IEEE International Geoscience and Remote Sensing Symposium*, pp. 1364-1367.
- Garthwaite, M., Miller, V., Saunders, S., Parks, M., Hu, G., Parker, A., 2019. A Simplified Approach to Operational InSAR Monitoring of Volcano Deformation in Low- and Middle-Income Countries: Case Study of Rabaul Caldera, Papua New Guinea. *Frontiers in Earth Science*, 6(240), pp. 1-23.
- Goldstein, R., Werner, C., 1998. Radar Interferogram Filtering for Geophysical Applications. *Geophysical Research Letters*, 25(21), pp.4035–4038.
- González, P, Bagnardi, M., Hooper, A., Larsen, Y., Marinkovic, P., Samsonov, S., Wright, T., 2015. The 2014–2015 Eruption of Fogo Volcano: Geodetic Modeling of Sentinel-1 TOPS Interferometry. *Geophysical Research Letters*, 42(21), pp.9239–9246.

- Grassi, F., Mancini, F., 2019. Sentinel-1 data for ground deformation monitoring: the SNAP-StaMPS workflow. In Workshop Tematico di Telerilevamento–Bologna, 25, pp.20-25.
- Grzesiak, K., Milczarek W., 2018. LOS Displacements of Mauna Loa volcano, Hawai-i Island, as Determined using SBAS-InSAR. E3S Web of Conferences, 55.
- Heliker, C., Swanson, D., Takahashi, T., 2003. The Pu'u O'o-Kupaianaha eruption of Kilauea Volcano, Hawai'i: the first 20 years. USGS Professional Paper 1676. US Geological Survey. Reston, Virginia, pp. 29-51.
- Hooper, A., Bekaert, D., Spaans, K., Arkan, M., 2012. Recent advances in SAR interferometry time series analysis for measuring crustal deformation. Tectonophysics, 514, pp.1-13.
- Hooper, A., Segall, P., & Zebker, H., 2007. Persistent scatterer interferometric synthetic aperture radar for crustal deformation analysis, with application to Volcán Alcedo, Galápagos. Journal of Geophysical Research: Solid Earth, 112(B7), B07407, pp. 1-21.
- Ihlen, V., 2019. Landsat 8 (L8) Data Users Handbook. U.S. Geological Survey, LSDS-1574, Version 5.0. Available online at: https://prd-wret.s3.us-west-2.amazonaws.com/assets/palladium/production/atoms/files/LSDS-1574_L8_Data_Users_Handbook-v5.0.pdf.
- Irish, R., 2000. Landsat 7 science data users handbook. National Aeronautics and Space Administration, Report, 2000, pp.415-430.
- Ji, L., Lu, Z., Dzurisin, D., Senyukov, S., 2013a. Pre-Eruption Deformation Caused by Dike Intrusion Beneath Kizimen Volcano, Kamchatka, Russia, Observed by InSAR. Journal of Volcanology and Geothermal Research, 256, pp.87–95.

- Ji, L., Xu, J., Wang, Q., & Wan, Y., 2013b. Episodic Deformation at Changbaishan Tianchi Volcano, Northeast China During 2004 To 2010, Observed by Persistent Scatterer Interferometric Synthetic Aperture Radar. *Journal of Applied Remote Sensing*, 7, 073499, pp.1-12.
- Jo, M., Jung, H. Won, J., 2017. Measurement of Precise Three-Dimensional Volcanic Deformations via TerraSAR-X Synthetic Aperture Radar Interferometry. *Remote Sensing of Environment*, 192, pp.228–237.
- Jo, M., Jung, H., Won, J., 2015a. Detecting the Source Location of Recent Summit Inflation via Three-Dimensional InSAR Observation of Kīlauea Volcano. *Remote Sensing*, 7(11), pp.14386-14402.
- Jo, M., Jung, H., Won, J., Lundgren, P., 2015b. Measurement of Three-Dimensional Surface Deformation by Cosmo-Skymed X-Band Radar Interferometry: Application to the March 2011 Kamoamoā Fissure Eruption, Kīlauea Volcano, Hawai'i. *Remote Sensing of Environment*, 169, 176-191.
- Kereszturi, G., Schaefer, L., Schleiffarth, W., Procter, J., Pullanagari, R., Mead, S., Kennedy, B., 2018. Integrating Airborne Hyperspectral Imagery and LiDAR for Volcano Mapping and Monitoring Through Image Classification. *International Journal of Applied Earth Observation and Geoinformation*, 73, pp.323–339.
- Kervyn, F., 2001. Modelling Topography with SAR Interferometry: Illustrations of A Favourable and Less Favourable Environment. *Computers and Geosciences*, 27(9), pp.1039–1050.

- Kobayashi, T., 2018. Locally Distributed Ground Deformation in an Area of Potential Phreatic Eruption, Midagahara Volcano, Japan, Detected by Single-Look-Based InSAR Time Series Analysis. *Journal of Volcanology and Geothermal Research*, 357, pp.213–223.
- Li, Z., Wright, T., Hooper, A., Crippa, P., Gonzalez, P., Walters, R., Elliot, J., Ebmeier, S., Hatton, E., Parsons, B., 2016. Towards InSAR Everywhere, All the Time, With Sentinel-1. *The International Archives of Photogrammetry, Remote Sensing and Spatial Information Sciences*, XLI-B4, pp. 763-766.
- Ji, L., Wang, Q., Qin, S., 2013. Present-Day Deformation of Agung Volcano, Indonesia, as Determined Using SBAS-InSAR. *Geodesy and Geodynamics*, 4(3), pp.65–70.
- Liu, L., Jafarov, E., Schaefer, K., Jones, B., Zebker, H., Williams, C., Rogan J., Zhang, T., 2014. InSAR Detects Increase in Surface Subsidence Caused By an Arctic Tundra Fire. *Geophysical Research Letters*, 41(11), pp.3906-3913.
- Lu, C., Ni, C., Chang, C., Yen, J., Chuang, R., 2018. Coherence difference analysis of sentinel-1 SAR interferogram to identify earthquake-induced disasters in urban areas. *Remote Sensing*, 10(8), pp.1-21.
- Lu, P., Bai, S., Tofani, V., Casagli, N., 2019. Landslides Detection Through Optimized Hot Spot Analysis on Persistent Scatterers and Distributed Scatterers. *ISPRS Journal of Photogrammetry and Remote Sensing*, 156, pp.147-159.
- Lu, Y., Ke, C.-Q., Zhou, X., Wang, M., Lin, H., Chen, D., Jiang, H., 2017. Monitoring Land Deformation in Changzhou City (China) with Multi-Band InSAR Datasets From 2006 to 2012. *International Journal of Remote Sensing*, 39(4), pp.1151-1174.

- Lu, Z., Dzurisin, D., Biggs, J., Wicks, C., McNutt, S., 2010. Ground Surface Deformation Patterns, Magma Supply, and Magma Storage at Okmok Volcano, Alaska, From InSAR Analysis: 1. Interruption Deformation, 1997–2008. *Journal of Geophysical Research: Solid Earth*, 115(B5), B00B02, pp.1-14.
- Lu, Z., Fatland, R., Wyss, M., Li, S., Eichelberger, J., Dean, K., Freymueller, J., 1997. Deformation of New Trident Volcano Measured by ERS-1 SAR Interferometry, Katmai National Park, Alaska. *Geophysical Research Letters*, 24(6), pp.695-698.
- Lu, Z., Rykhus, R., Masterlark, T., Dean, K., 2004. Mapping Recent Lava Flows at Westdahl Volcano, Alaska, Using Radar and Optical Satellite Imagery. *Remote Sensing of Environment*, 91(3), pp.345–353.
- Lu, Z., Wicks, C., Dzurisin, D., Thatcher, W., Freymueller, J., McNutt, S., Mann, D., 2000. Aseismic Inflation of Westdahl Volcano, Alaska, Revealed by Satellite Radar Interferometry. *Geophysical Research Letters*, 27(11), pp.1567–1570.
- Lundgren, P.R., Bagnardi, M., Dieterich, H., 2019. Topographic Changes During the 2018 Kīlauea Eruption from Single-Pass Airborne InSAR. *Geophysical Research Letters*, 46(16), pp.9554–9562.
- Miao, J., Zhou, X., Huang, T., Zhang, T., Zhou, Z., 2019. A Novel Inpainting Algorithm for Recovering Landsat-7 ETM+ SLC-OFF Images Based on the Low-Rank Approximate Regularization Method of Dictionary Learning with Nonlocal and Nonconvex Models. *IEEE Transactions on Geoscience and Remote Sensing*, 57(9), pp.6741-6754.
- Morgan, W. 1971. Convection Plumes in the Lower Mantle. *Nature*, 230, pp.42–43.

- Mouginis-Mark, P., Garbeil, H., 2005. Quality of TOPSAR Topographic Data for Volcanology Studies at Kīlauea Volcano, Hawaii: An Assessment Using Airborne LiDAR Data. *Remote Sensing of Environment*, 96(2), pp.149–164.
- Neal, C., Brantley, S., Antolik, L., Babb, J., Burgess, M., Calles, K., Cappos, M., Chang, J., Conway, S., Desmither, L., Dotray, P., 2019. The 2018 Rift Eruption and Summit Collapse of Kīlauea Volcano. *Science*, 363(6425), pp.367-374.
- Parks, M., Biggs, J., Mather, T., Pyle, D., Amelung, F., Monsalve, M., Medina, L., 2011. Co-Eruptive Subsidence at Galeras Identified During an InSAR Survey of Colombian Volcanoes (2006–2009). *Journal of Volcanology and Geothermal Research*, 202(3), pp.228-240.
- Pepe, A., Calò, F., 2017. A Review of Interferometric Synthetic Aperture RADAR (InSAR) Multi-Track Approaches for the Retrieval of Earth's Surface Displacements. *Applied Sciences*, 7(12), pp.1-39.
- Plank, S., Walter, T., Martinis, S., Cesca, S., 2019. Growth and Collapse of a Littoral Lava Dome During the 2018/19 Eruption of Kadovar Volcano, Papua New Guinea, Analyzed by Multi-Sensor Satellite Imagery. *Journal of Volcanology and Geothermal Research*, 388, 106704, pp.1-15.
- Poland, M., Lu, Z., 2008. Radar interferometry observations of surface displacements during pre- and co-eruptive periods at Mount St. Helens, Washington, 1992-2005. Chapter 18 in *A volcano rekindled: the renewed eruption of Mount St. Helens, 2004-2006*, US Geological Survey, 1750(18), pp. 361-382.

- Poland, M.P., 2014. Time-Averaged Discharge Rate of Subaerial Lava at Kīlauea Volcano, Hawai'i, Measured from Tandem-X Interferometry; Implications for Magma Supply and Storage During 2011-2013. *Journal of Geophysical Research: Solid Earth*, 119(7), pp.5464–5481.
- Pritchard, M., Henderson, S., Jay, J., Soler, V., Krzesni, D., Button, N., Welch, M., Semple, A., Lass, B., Sunagua, M., Minaya, E., Amigo, A., Clavero, J., 2014. Reconnaissance Earthquake Studies at Nine Volcanic Areas of The Central Andes with Coincident Satellite Thermal and InSAR Observations. *Journal of Volcanology and Geothermal Research*, 280, pp.90–103.
- Reuter, D., Richardson, C., Pellerano, F., Irons, J., Allen, R., Anderson, M., Jhabvala, M., Lunsford, A., Montanaro, M., Smith, R., 2015. The Thermal Infrared Sensor (TIRS) on Landsat 8: Design Overview and Pre-Launch Characterization. *Remote Sensing*, 7(1), pp.1135-1153.
- Richter, N., Poland, M., Lundgren, P., 2013. TerraSAR-X Interferometry Reveals Small-Scale Deformation Associated with the Summit Eruption of Kīlauea Volcano, Hawai'i. *Geophysical Research Letters*, 40(7), pp.1279–1283.
- Rowland, S., MacKay, M., Garbeil, H., Mougini-Mark, P., 1999. Topographic Analyses of Kilauea Volcano, Hawai'i, from Interferometric Airborne Radar. *Bulletin of Volcanology*, 61(1), pp.1-14.
- Schroeder, W., Oliva, P., Giglio, L., Csiszar, I., 2014. The New VIIRS 375m Active Fire Detection Data Product: Algorithm Description and Initial Assessment. *Remote Sensing of Environment*, 143, pp.85-96.

- Shaw, H., Wright, T., Peck, D., Okamura, R., 1968, The Viscosity of Basaltic Magma: An Analysis of Field Measurements in Makaopuhi Lava Lake, Hawaii. *American Journal of Science*, 266, pp.225- 264.
- Shirzaei, M., Bürgmann, R., Foster, J., Walter, T., Brooks, B., 2013(a). Aseismic Deformation Across the Hilina Fault System, Hawaii, Revealed by Wavelet Analysis of InSAR and GPS Time Series. *Earth and Planetary Science Letters*, 376, pp.12-19.
- Shirzaei, M., Walter, T., Bürgmann, R., 2013(b). Coupling of Hawaiian volcanoes only during overpressure condition. *Geophysical Research Letters*, 40(10), pp.1994-1999.
- Sigmundsson, F., Durand, P. Massonnet, D., 1999. Opening of an Eruptive Fissure and Seaward Displacement at Piton de la Fournaise Volcano Measured by RADARSAT Satellite Radar Interferometry. *Geophysical Research Letters*, 26(5), pp.533–536.
- Thompson, J., Ramsey, M., 2020. Uncertainty Analysis of Remotely-Acquired Thermal Infrared Data to Extract the Thermal Properties of Active Lava Surfaces. *Remote Sensing*, 12(193), pp.1-21.
- Tofani, V., Raspini, F., Catani, F., Casagli, N., 2013. Persistent Scatterer Interferometry (PSI) Technique for Landslide Characterization and Monitoring. *Remote Sensing*, 5(3), pp.1045-1065
- Torres, R., Snoeij, P., Geudtner, D., Bibby, D., Davidson, M., Attema, E., Potin, P., Rommen, B., Floury, N., Brown, M., Traver, I., Deghaye, P., Duesmann, B., Rosich, B., Miranda, N., Bruno, C., L'Abbate, M., Croci, R., Pietropaolo, A., Huchler, M., Rostan, F., 2012. GMES Sentinel-1 Mission. *Remote Sensing of Environment*, 120, pp.9-24.

USGS (2018a): Kilauea Volcano, June HI 2018 Acquisition airborne LiDAR survey. U.S.

Geological Survey (USGS) in Collaboration with GEO1, Windward Aviation, Quantum Spatial, and Cold Regions Research and Engineering Laboratory. Distributed by OpenTopography. <https://doi.org/10.5069/G98K7718>. Accessed: 2020-03-19

USGS (2018b): Kīlauea Volcano, HI July 2018 Acquisition airborne LiDAR survey. U.S.

Geological Survey (USGS) in collaboration with the State of Hawaii, Federal Emergency Management Agency, Cold Regions Research and Engineering Laboratory, and the National Center for Airborne Laser Mapping. Distributed by OpenTopography. <https://doi.org/10.5069/G9M32SV1>. Accessed: 2020-03-19.

Wang, T., Degrandpre, K., Lu, Z., Freymueller, J., 2018. Complex Surface Deformation of Akutan Volcano, Alaska Revealed from InSAR Time Series. *International Journal of Applied Earth Observation and Geoinformation*, 64, pp.171–180.

Welch, M., & Schmidt, D., 2017. Separating Volcanic Deformation and Atmospheric Signals at Mount St. Helens Using Persistent Scatterer InSAR. *Journal of Volcanology and Geothermal Research*, 344, pp.52-64

Wessels, R., Vaughan, R., Patrick, M., Coombs, M., 2013. High-Resolution Satellite and Airborne Thermal Infrared Imaging of Precursory Unrest and 2009 Eruption at Redoubt Volcano, Alaska. *Journal of Volcanology and Geothermal Research*, 259, pp.248–269.

Wnuk, K., Wauthier, C., 2017. Surface Deformation Induced by Magmatic Processes at Pacaya Volcano, Guatemala Revealed by InSAR. *Journal of Volcanology and Geothermal Research*, 344, pp.197–211.

Wulder, M., Masek, J., Cohen, W., Loveland, T., Woodcock, C., 2012. Opening the Archive: How Free Data Has Enabled the Science and Monitoring Promise of Landsat. *Remote Sensing of Environment*, 122, pp.2-10.

Zhai, G., Shirzaei, M., 2016. Spatiotemporal Model of Kīlauea's Summit Magmatic System Inferred from InSAR Time Series and Geometry-Free Time-Dependent Source Inversion. *Journal of Geophysical Research: Solid Earth*, 121(7), pp.5425–5446.

Zhang, Z., Wang, C., Tang, Y., Fu, Q., Zhang, H., 2015. Subsidence Monitoring in Coal Area Using Time-Series InSAR Combining Persistent Scatterers and Distributed Scatterers. *International journal of applied earth observation and geoinformation*, 39, pp.49-55.

Zhou, X., Chang, N., Li, S., 2009. Applications of SAR Interferometry in Earth and Environmental Science Research. *Sensors*, 9, pp.1876-1912.

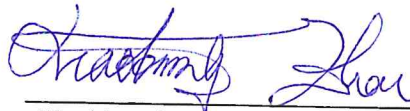
Web References

1. ESA. Sentinel-1Acquisition modes. <https://sentinel.esa.int/web/sentinel/user-guides/sentinel-1-sar/acquisition-modes> (accessed 19 February 2020).
2. ESA. Copernicus program. <https://disasters.nasa.gov/programs/esa-copernicus> (accessed 19 February 2020).
3. ESA. Sentinel-1A imagery. <https://scihub.copernicus.eu/dhus/#/home> (accessed 19 February 2020).
4. GOHAWAII. Weather information at Hawaii. <https://www.gohawaii.com/trip-planning/weather> (accessed 19 February 2020).

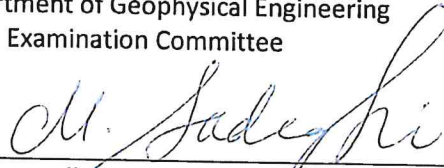
5. Kīlauea LiDAR, 2018. Information of LiDAR data acquisition over the Kīlauea volcano in 2018. <https://Kīlauealidar.com/> (accessed 19 February 2020).
6. NASA, 2020. About Landsat program. <https://landsat.gsfc.nasa.gov/about/> (accessed 19 February 2020).
7. NASA. Fire Information and Resource Management System data. <https://firms.modaps.eosdis.nasa.gov/download/> (accessed 19 February 2020).
8. Opentopography. LiDAR imagery. <http://opentopo.sdsc.edu/datasets.jsp> (accessed 19 February 2020).
9. PRWeb, 2018. News about Quantum Spatial providing high resolution LiDAR data over the Kīlauea volcano. <https://www.prweb.com/releases/2018/07/prweb15614885.htm> (accessed 19 February 2020). Written by Maria Bradley. 10 July 2018.
10. US News, 2019. News article about record-breaking temperatures in Hawaii. <https://www.usnews.com/news/best-states/articles/2019-09-27/hawaii-saw-record-breaking-temperatures-this-summer>. (accessed 19 February 2020). Written by Casey Leins. 27 September 2019.
11. USGS, 2020. Information about Landsat 7. https://www.usgs.gov/land-resources/nli/landsat/landsat-7?qt-science_support_page_related_con=0#qt-science_support_page_related_con (accessed 19 February 2020).
12. USGS. Landsat 7 imagery. <https://earthexplorer.usgs.gov/> (accessed 19 February 2020).
13. USGS. Landsat 8 imagery. <https://earthexplorer.usgs.gov/> (accessed 19 February 2020).

SIGNATURE PAGE

This is to certify that the thesis prepared by Ninad Bhagwat entitled "Monitoring the 2018 Eruption of the Kilauea Volcano Using Various Remote Sensing Techniques" has been examined and approved for acceptance by the Department of Geophysical Engineering, Montana Technological University, on this 29th day of July, 2020.

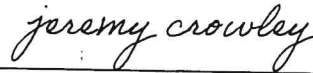


Xiaobing Zhou, PhD, Professor
Department of Geophysical Engineering
Chair, Examination Committee

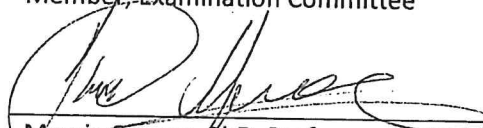


Mohammadhussain Sadeghianirshahidi, PhD, Assistant Professor
Department of Geological Engineering
Member, Examination Committee

Jeremy Crowley



Jeremy Crowley, MS, GISP, PG, Hydrogeologist and Assistant Research
Professor
Montana Bureau of Mines and Geology
Member, Examination Committee



Marvin Speece, PhD, Professor and Department Head
Department of Geophysical Engineering
Member, Examination Committee